Q-plate technology: a progress review [Invited]

ANDREA RUBANO,* **FILIPPO CARDANO,** [ID] **BRUNO PICCIRILLO,** [ID] **AND LORENZO MARRUCCI**

Universitá di Napoli Federico II, Dipartimento di Fisica "Ettore Pancini", Complesso Universitario di Monte S. Angelo, via Cintia, Napoli, Italy
Corresponding author: andrea.rubano@fisica.unina.it

Since their first introduction in 2006, *q*-plates have found a constantly increasing number of uses in diverse contexts, ranging from fundamental research on complex structured light fields to more applicative innovations of established experimental techniques, passing through a variety of other emerging topics, such as, for instance, quantum information protocols based on the angular momentum of light. In this paper, we present a bird's-eye view of the progress of this technology in recent years and offer some educated guesses on the most likely future developments.   © 2019 Optical Society of America

1. INTRODUCTION

A rigid body can exhibit two kinds of rotations: it can spin around its axis and it can rotate around a distant point. For instance, a planet spins around its axis and rotates around the Sun. These two kinds of rotations can be associated with distinct contributions to the conserved quantity angular momentum, respectively, known as spin angular momentum (SAM) and orbital angular momentum (OAM). The former reflects an internal state of the object, while the latter regards its overall motion in space. A similar distinction can be made at a subatomic level when describing the motion of an electron around the nucleus. The electron being a point particle (to the best of our knowledge), one cannot truly talk of electron "rotation" around its axis. Yet, the electron is known to possess a well-defined SAM, described by a definite quantum number. A similar concept can be applied to photons, for which the SAM is associated with the polarization state of light, while the OAM is controlled by the wavefront shape in space. In the wave representation, a photon with a non-vanishing OAM quantum number will be represented by a wave function having a helical wavefront, whereas, in the particle representation, that photon will "twist" around its direction of propagation as it moves forward. For photons, the distinct physical meaning of the two angular momentum terms can be non-obvious at first sight, but it can be straightforwardly proven by experiments in which a nanoscale free particle is forced to rotate around its axis or around an external point by the interaction with SAM- or OAM-carrying photons, respectively [1,2]. It is then possible to say that there is an exchange of each form of angular momentum between the photons and the particle. While the manipulation of light polarization in standard Gaussian beams is something routinely done in laboratories, the technology that allows one to arbitrarily shape the optical field spatial structure, including polarization and phase, has matured only in recent years—a research area nowadays known as "structured light". The topic of the light OAM, and more generally of singular optics, with its complex helical phase or polarization structures, is inextricably linked to the technology of structured light, including diffractive waveplates and similar devices, which are the main subject of this special issue.

The most straightforward method to implement an arbitrary wavefront reshaping is by introducing optics that make the optical path-length of the light beam vary across the beam transverse section, hence adding to the beam a spatially variant phase shift. This is achieved, for instance, by using a spiral phase plate or a spatial light modulator (SLM) [3]. A totally different approach, which is what we are mainly interested in here, relies instead on the concept of Pancharatnam–Berry (PB) phases [4–10], which are phase shifts arising when the local polarization state of light is subjected to suitable transformations.

Q-plates were invented in 2006 starting from general considerations on the SAM and OAM exchanges that occur in inhomogenous anisotropic media, such as patterned liquid crystals (LCs) [6,7]. A *q*-plate is a LC device having an azimuthal pattern of the LC molecular director around a central point. The *q*-plate pattern is characterized mainly by the topological charge *q* of the central singularity, which can be an integer or half-integer. A *q*-plate with $q = 1$, which has global rotational symmetry with respect to its center, leads to an exact conversion of the SAM variation into OAM, within the same light beam, without any net angular momentum exchange with the medium. This process is called spin-to-orbital angular momentum conversion [6]. More generally, *q*-plates of arbitrary topological charge *q* allow generating light beams carrying an OAM of $\pm 2q\hbar$ per photon, with the OAM sign controlled by the input polarization helicity. The working principle of *q*-plates can be best explained in terms of the PB phases generated by the patterned LC birefringence, and therefore *q*-plates

are among the first examples of PB-based optical phase elements operating in the visible domain. In this respect, they represent an evolution of the mid-infrared-domain subwavelength-grating devices introduced in 2002 by Hasman and coworkers [5] (but these earlier works did not refer explicitly to the angular momentum transformations).

More generally, the technology at the base of q-plates can be extended to cover not only the case of beams with well-defined spiral wavefront and well-defined circular polarization (i.e., pure OAM and SAM eigenstates) but also more complex non-separable structures of wavefront and local polarization, such as, e.g., those falling in the class of vector–vortex beams. The study of complex structured light could be regarded as a renaissance of old-school classical optics, as many of its phenomena have been revisited with novel results [11]. Its implications, however, are much broader than this: for instance, new exciting playgrounds for quantum protocols based on twisted photons [12] have been created, or the possibility to generate three-dimensional complex field structures, such as the Möbius strips of optical polarization [13].

The technological advantages of using q-plates instead of other technologies for producing structured light beams are many: (i) the conversion efficiency (ratio of OAM-converted light power over total transmitted light power) is very high, with >97% routinely achieved; reflection losses currently limit the overall q-plate transmission to ~85%, but this figure could be improved significantly with a standard anti-reflection coating; (ii) the device is compact and stable, also in the long term, and requires minimum to no maintenance; (iii) the device works in transmission geometry and therefore is free of many alignment problems; (iv) the q-plate does not deflect the beam (unlike holographic methods) and hence does not introduce astigmatism; (v) it can be used in a wide range of frequencies and also with ultra-short pulses [14]; (vi) electrical control can switch the device on and off or tune in general the plate for optimal operation at different wavelengths or for deliberately introducing partial OAM conversion; (vii) the device can be used to create superpositions of SAM/OAM states without using interferometric setups; and (viii) several q-plates can be arranged in cascade to be able to address a large range of OAM values.

In this paper, we will review a range of applications in which q-plate have been used to generate structured light beams, carrying OAM or featuring complex polarization topologies, focusing mainly on the progress occurring in the last 5–7 years. Due to the very large literature that has been produced in the last years, we had to make choices, and the presented collection is likely not exhaustive. Yet, we hope that the most representative works for each field of research here revised have been included.

The paper is organized as follows: in Section 2, the working principle of the q-plate is briefly recalled, and the main advances in the q-plate fabrication process and operation procedures are summarized; in Section 3, we survey recent works that exploit q-plates for OAM states generation and controlled manipulation; in Section 4, we review works that exploit the use of q-plates to generate vector beams, which are specific superpositions of SAM/OAM eigenstates; in Section 5, works

concerning more complex structured light beams, e.g., involving infinite eigenstates of OAM, are discussed; in Section 6 we review those works which are mainly focused on the fundamental physics of structured beams, such as for instance three-dimensional polarization geometries of highly non-paraxial beams. Finally, in the Conclusion (Section 7), we try to outline the scope of possible future applications of q-plate technology for the coming years.

2. *Q*-PLATE WORKING PRINCIPLE AND FABRICATION

The q-plate is essentially a LC cell, i.e., a thin (nematic) LC film sandwiched between two coated plane glasses. LCs are anisotropic (hence birefringent) fluids, with a nonrandom average local molecular orientation, usually specified by a unit vector **n** called molecular director. Unlike standard LC cells, which have a uniform director across the plate, a q-plate has a specific azimuthal pattern of **n** in the cell plane, with the azimuthal coordinate defined with respect to a central point, taken to be the coordinate origin.

In more detail, the angle α between **n** and a fixed reference axis in the cell plane, which can be identified with the x-coordinate axis, is a linear function of the azimuthal angle ϕ in the plane:

$$\alpha(\phi) = q\phi + \alpha_0. \tag{1}$$

The coefficient q appearing in this expression is the topological charge, and the intercept α_0 is the angle of the LC director on the reference x axis. The angle α is instead taken to be independent of the radial coordinate r giving the distance from the origin. Equation (1) can be read as follows: in any circular counterclockwise path around the origin, the LC director **n** makes exactly q turns around itself. q can also be negative if the **n** rotation is clockwise. Moreover, q can be half-integer because **n** is physically equivalent to −**n**, i.e., the LC molecular director is a non-polar axis. This pattern can be written on the coating layer of the cell before introducing the LC in the cell, by means of different techniques. The most powerful and versatile one consists of the photo-alignment of dye molecules in the coating layers [15], which will then force the LC molecules to follow the same alignment.

As mentioned, the coefficient q in Eq. (1) is the topological charge that characterizes the central pattern singularity, and the OAM quantum number that a q-plate generates is $\pm 2q$, while α_0 affects only the global phase of the emerging light. Another important parameter of the q-plate is the total birefringent phase retardation δ of the LC film. This is a function of film thickness and LC birefringence, but can also be modulated by an applied electric field (which tilts the molecular director away from the transverse plane of the q-plate, thus reducing the effective birefringence seen by light) [16]. This is a particularly convenient feature of q-plates built with thermotropic (non-polymeric) LCs, which sets them apart from other diffractive-waveplate technologies. A first trivial consequence of this, e.g., is that one can literally turn on and off the plate with minimal to no change on any other optical parameter. A more detailed view of the q-plate layered structure can be seen in Fig. 1, where the layers are disjointed (panel a) for clarity. A real device
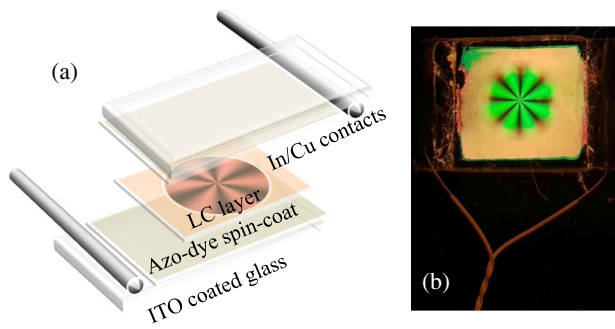
Fig. 1. Explosion of the *q*-plate layers (a) and a crossed-polarizer image of a real device (b). The lateral size is about 2 cm.

is presented in panel b, which shows the appearance of a *q*-plate if observed between crossed polarizers. A natural light image would show just a transparent piece of glass with wires, but when looking at the plate between two crossed polarizers, the LC birefringent azimuthal pattern becomes visible. The reason for the colored pattern is that the birefringent phase retardation is wavelength dependent, besides depending on temperature and other building parameters (mainly cell thickness). While operating the *q*-plate, this effect is under control by electrical tuning.

A. Q-Plate Fabrication

Several technical advances have been introduced since the first *q*-plate was built in 2006. The most important is clearly the photo-alignment method. The photo-alignment method here described [15–17] allows one to obtain, in principle, any integer and semi-integer, positive or negative *q* value, with an upper limit to the absolute value |*q*|, which depends only on technological constraints and protocols. This flexibility is ensured by the photo-alignment procedure, which enables one to write on the plate any pattern, provided it has an azimuthal cylindrical symmetry. More generally, masks and other more refined techniques may allow one to obtain a totally generic pattern, and thus to explore even more the space of complex beams that can be produced with this method. A simplified schematic of the experimental setup is shown in Fig. 2.

Two indium-tin oxide (ITO)-coated glass substrates form the cell that will host the LC. ITO is a well-known transparent conductor, whose role in the cell will be explained in the following. Before building the cell, each glass substrate is
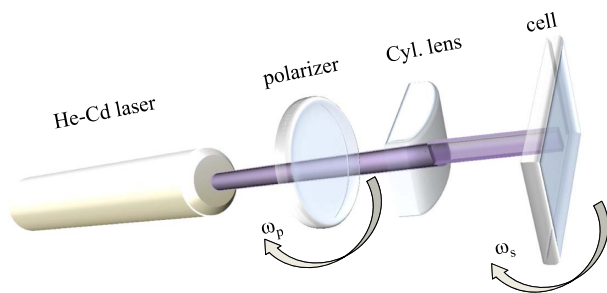
Fig. 2. Sketch of the photo-alignment setup (strongly simplified). The illuminating polarization and the cell are both rotated in time with independent step-wise angular velocity, as indicated by arrows.

spin-coated (on the ITO-coated side) with a solution of a photosensitive sulphonic azo-dye, and then heated for several minutes for evaporating the solvent. The thickness of the cell is a crucial parameter for *q*-plate operation, and its value should be small but very precise and uniform. To achieve this, dielectric micro-spacers (with 6 μm average thickness) are inserted between the two coated glasses before gluing them together so as to obtain an empty LC cell, with two sides of the cell left open for the subsequent LC filling. The next step is the writing of the orientation pattern on the azo-dye layer. When exposed to light with wavelengths in the blue or near UV, the azo-dye surfactant tends to reorient along a direction perpendicular to light polarization. This photo-alignment process is quite critical, and the result depends on light intensity, wavelength, exposure time, and many other details. But, if done properly, the resulting LC surface anchoring energy is comparable with the polyimide-rubbing-based alignment used in most LC technology. For this photo-alignment stage, we currently use a He–Cd laser emitting at a wavelength of 325 nm. The laser beam is polarization controlled by a half-wave-plate polarizer and then sent to a cylindrical lens, which creates a "brush of light" to illuminate only a narrow angular sector of the cell. The half-wave-plate polarizer and the sample are rotated stepwise by means of remote-controlled motorized mounts. At each angular step, a suitable exposure time is then needed to obtain stable dye alignment. By choosing the ratio between the angular rotations of the two motors, one writes the pattern needed to obtain a specific *q* value. It can be easily shown that the induced topological charge is given by $q = 1 \pm \omega_p/\omega_s$, where ω_p and ω_s are the angular speeds of the polarization and sample, respectively, and the ± sign corresponds to opposite (+) or same (−) rotation directions of the two mounts. Values of the topological charge ranging up to $q = 50$ have been achieved by this method. After exposure, the plates are filled with the LC and sealed on the remaining open sizes by epoxy glue. Heating the sample above the LC clearing point and subsequent slow cooling helps removing occasional LC alignment defects.

B. Q-Plate Electrical Control: Tuning

When building the cell, the two glasses are set in a slightly shifted relative position, as shown in Fig. 1(a), in order to be able to access the ITO-coated surface on both sides. Once the cell is sealed, two copper wires are welded with indium to the ITO thin film. As mentioned, by adjusting the AC voltage applied to the electrodes, it is possible to achieve full control of the birefringent phase retardation δ for a given operation wavelength and temperature.
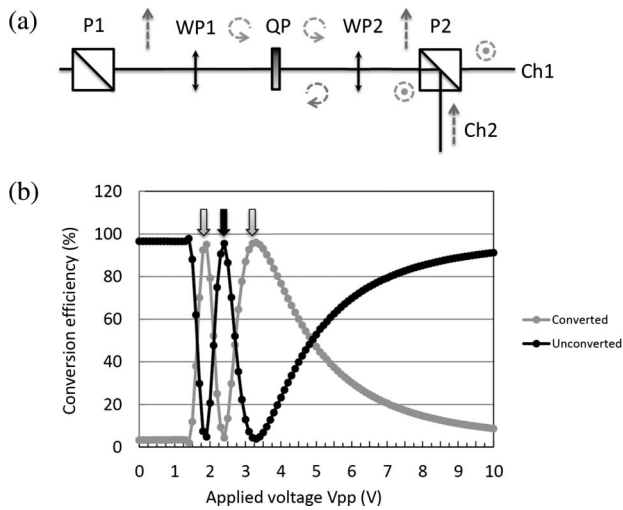
When a beam traverses a *q*-plate with topological charge *q* and phase retardation δ, a fraction $\sin^2(\delta/2)$ of the photons in the beam has its SAM reversed and changes its OAM by an amount $\pm 2q$. The remaining photon fraction $\cos^2(\delta/2)$ remains in its initial SAM and OAM states. Representing the left and right polarization states with the bracket notation, we can define the operation of the *q*-plate by means of the unitary operator $\hat{U}$, defined as follows:

$$\begin{cases} \hat{U}|L\rangle = \cos(\delta/2)|L\rangle + \mathrm{i}\sin(\delta/2)|R\rangle\mathrm{e}^{+2\mathrm{i}\alpha(\phi)}, \\ \hat{U}|R\rangle = \cos(\delta/2)|R\rangle + \mathrm{i}\sin(\delta/2)|L\rangle\mathrm{e}^{-2\mathrm{i}\alpha(\phi)}. \end{cases} \quad (2)$$

When the phase retardation of the q-plate is tuned to half-wave ($\delta = \pi$) the first term vanishes, and all the input photons are converted from right (left) to left (right) polarization and gain a helical phase $\pm 2\alpha(\phi) = \pm 2(q\phi + \alpha_0)$. In the particular case of charge $q = 1$, the total SAM + OAM angular momentum remains unchanged when the beam passes through the q-plate, so that the change of the photon SAM is transferred entirely into a corresponding opposite change of the photon OAM, yielding a full spin-to-OAM conversion [6,7].

A simple way of measuring the conversion efficiency associated with this process is shown in Fig. 3(a), where a linear polarization is transformed into circular by a first quarter-wave plate (WP1) then converted by the q-plate (QP) and then rotated back to linear by a second quarter-wave plate (WP2), and finally split by a polarizer (P2) in two separate channels. The light intensity on each channel then gives a measure of the amount of converted/unconverted light. The result of a typical experiment is shown in Fig. 3(b), where the two channels are shown as a function of the AC voltage applied to the plate (AC voltage is necessary in LC cell control to avoid charge accumulation, but the frequency within a given large range of tolerance is irrelevant). In the figure, each channel light intensity is normalized to the sum of the two. The conversion efficiency, which is the ratio between the intensity of converted light and total output intensity, is typically around 97%–98% at the peak.

The white (black) arrows indicate the points of maximum (minimum) of conversion efficiency. Switching between these voltage values can thus turn, for instance, a left (right) circular polarization OAM = 0 mode into a right (left) circular polarization OAM = $2q$ (OAM = –$2q$) mode, as depicted in Fig. 4, with no change in any other optical parameter. In the figure, the q-plate is depicted by using lines that are parallel to the LC local molecular director. In this representative case, the line orientation rotates by π when circling once around the center, thus realizing a $q = 1/2$ topological charge. The electric field tuning has, however, many more applications than just the switching between OAM states, as it will be clarified in the subsequent sections of this paper.


Fig. 3. Experimental configuration for q-plate tuning (a) and the results observed on the two output channels (b). P1,2, polarizing beamsplitters; WP1,2 quarter-wave plates; QP, q-plate.

3. ORBITAL ANGULAR MOMENTUM GENERATION AND MANIPULATION AND RELATED APPLICATIONS

The most straightforward applications of the q-plate are for generating optical beams carrying OAM starting from ordinary Gaussian beams, or for modifying the input OAM according to prescribed laws. In this, q-plates are similar to ordinary spiral phase plates, but with several advantages, such as polarization control of the OAM variation, electrical switching, and tuning, multiple wavelength operation, etc.

A particularly good example of the special opportunities offered by the possibility of electrically tuning the q-plate phase retardation δ (which goes far beyond the simple on–off schemes) is provided in a work by Yan and coworkers [19] about stimulated emission depletion (STED) nanoscopy. STED is a very popular technique for far-field imaging that
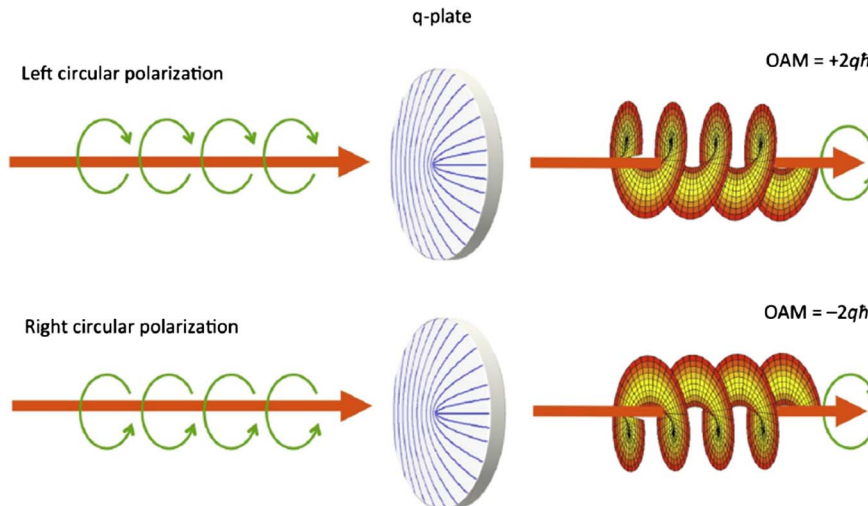
Fig. 4. *Q*-plate working principle; a pictorial representation of Eq. (2) in the optimal case $\delta = \pi$ (reprinted with permission from Ref. [18]).

(a)   (b)

(c)
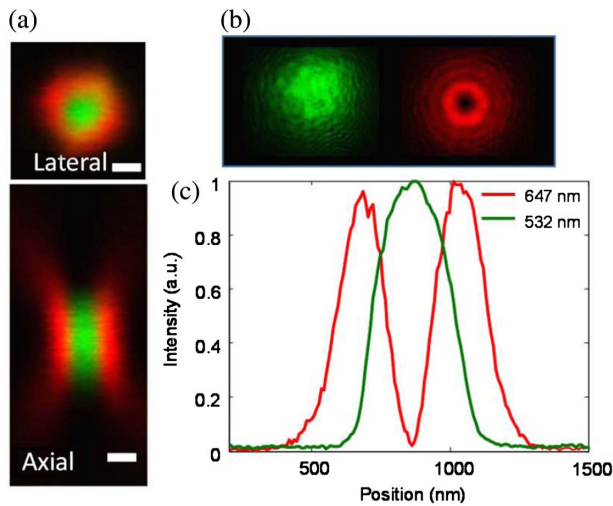
Fig. 5. Two-color beam generated by a *q*-plate and used for STED nanoscopy, on the transverse and axial planes (a) and the corresponding free-space separate beams (b). Panel (c) shows a cut on the transverse plane along the central line (reprinted with permission from Ref. [19]).

bypasses the diffraction limit of light microscopy to increase optical resolution. It works by depleting the fluorescence in specific regions of the sample while leaving a central focal spot active to emit. This peculiar effect can be achieved by means of an inhomogeneous two-color beam having one color in the center and the second color around it, in a doughnut shape. Conventional STED requires one to align very precisely the excitation and the doughnut beams on a common axis, which is a demanding requirement for practical devices. With *q*-plates, the two-color beam can be achieved directly on a single optical line. Two beams at different wavelengths $\lambda_{1,2}$ are indeed mixed together in a fiber coupler with polarization controls and then sent to the *q*-plate. Since the phase retardation δ depends on λ, it is possible, by suitable choices of the wavelengths, to find a bias voltage that minimizes conversion efficiency for one color and maximizes it for the other, at the same time. Figure 5(b) shows the two beams separately for a given value of the AC tuning voltage, while Fig. 5(a) shows them together. Figure 5(c) finally shows that the extinction of the doughnut beam in the center (which is obviously a critical parameter to achieve good STED imaging) is good enough (>18 dB) for STED applications. Moreover, the same concept has been proven to work for a three-color beam (two in the center and one in the doughnut), so that multiple fluorescent emitters can be used to reconstruct the image with a super-continuum white-light generation source, allowing for using the *q*-plate in combination with single-mode optical fibers as a wavelength selective optical filter, or optical switch, to move between different frequency channels [20].

A. Classical Communication with OAM Beams

Possibly the first connection between *q*-plates and classical information manipulation was given in a work in 2012 [21], in which Karimi and coworkers demonstrated the possibility of converting OAM-encoded information into time-bin encoding

or vice versa by exploiting a *q*-plate inserted in a ring cavity. At each round-trip in the cavity, a femtosecond light pulse goes through the *q*-plate and shifts its OAM by $\pm 2q$. By setting the round-trip time, it is then possible to separate in time light pulses having different OAM values or generating different OAM values at different times, thus realizing a time-division multiplexing of OAM. This work was carried out in free space.

The key technology for optical communication is, however, that of optical fibers. In this area, *q*-plates have been recently used as higher-order polarization controllers for coupling free-space optical beams to specific higher-order fiber modes, in particular in the case of OAM fibers. An OAM fiber (or vortex fiber) is a specially designed optical fiber that is able to transport the OAM of light with little crosstalk to other modes. The *q*-plate has been demonstrated to be an ideal tool for exciting pure fiber modes of such fibers due to its simple geometry and large efficiency [22]. In more recent years, technological advances in the field of fiber manufacturing has made it possible to transmit simultaneously up to 12 independent OAM modes [23] over a distance of >1 km with sufficiently low crosstalk, and there is room for increasing this number at least by a further factor two with present technology. Mode-division multiplexing makes use of different modes supported by the fiber to encode separate channels, as long as these modes do not interact too strongly with each other. In normal fibers, the OAM modes are strongly coupled owing to perturbations and fiber bending because of their near degeneracy in frequency. It is possible to compensate these effects by digital processing, but at increasing costs in terms of time and energy of the compensation process, which effectively limits the number of modes one can couple in the fiber and detect at the output with a sufficiently small amount of errors. Special fiber designs allow now to couple more and more modes with minimal crosstalk, and thus the OAM-based mode multiplexing is getting closer to market-ready applications.

B. Quantum Information Technologies

Q-plates have been used as angular momentum converters for studying the dynamics of vortices (topological defects occurring in macroscopically coherent systems) created in quantum fluids, such as polariton condensates [24,25]. *Q*-plates have been employed in quantum optics also to prove the experimental violation of Leggett-type inequalities for a hybrid entangled state of SAM and OAM of a single photon [26] and to demonstrate a scheme to generate non-coherent and coherent correlations, i.e., a tunable degree of entanglement, between degrees of freedom of a single photon [27]. Another important application of this technology in the area of quantum physics is the simulation of quantum dynamics, such as quantum walks, which will be reviewed separately in the next subsection.

In order to encode any kind of information into any kind of physical system able to carry this information from one place to another, one needs to define "states" and to define how to translate the information on those states. In the standard electrical-circuit approach, a state can simply be voltage on–off, so as to encode the message according to a binary Boolean algebra. A similar thing can be done with light, e.g., if one chooses the horizontal/vertical linear polarizations or the left/right circular

polarizations as binary bases. This will represent a bit. In quantum information, the bit is replaced by a qubit, i.e., the state of the system is meant to be a quantum state. The qubit can be considered as the elementary unit of quantum information. It is possible to do so, for instance, with electrons (spin up/down) or with photons (right/left). In the latter case, a single photon can carry both states in a quantum superposition, and therefore it defines a qubit. One can actually think of enlarging the number of available states to more than two on a single photon, and this unit of quantum information in a high-dimensional space takes the name of qudit. It is evident that one can store a much larger amount of information per photon in such high-dimensional systems, and therefore it would be appealing to be able to create and manipulate those systems in a simple way. The *q*-plate actually gives a handy tool for this, as the OAM state of light can be used to encode information [12], and the OAM quantum number is (in principle) infinite. The difficulties in generating and manipulating OAM states, however, can make a typical quantum experiment (where optical phases are usually critical) much more demanding. For example, a classic two-photon quantum interference process such as the Hong–Ou–Mandel effect was not demonstrated until recently for photons carrying non-zero OAM. The Hong–Ou–Mandel effect has played a crucial role in many landmark advances of quantum information technology, such as, for instance, quantum teleportation [29,30]. This effect consists, in brief, of a destructive interference of equivalent outputs of indistinguishable photons following different paths, as in Feynman's interpretation of quantum theory. In particular, when two photons impinge on a 50% beam splitter from two different sides, they will always emerge from the beam splitter and be detected on the same side (i.e., one reflected and one transmitted), while the possibility that the two photons emerge from two distinct sides (i.e., they are both reflected or both transmitted) is entirely suppressed by interference, as long as they are indistinguishable. If the two photons have different internal quantum states, i.e., different polarization or other degrees of freedom, the effect vanishes, as seen in Fig. 6 [31]. The Hong–Ou–Mandel effect can be used to create an optimal quantum-cloning machine, because if one of the two photons is the one to be cloned and the other one is random, the pair at the output of the beam splitter (on both sides) will present a larger probability that the two are identical with respect to the case in which they are not. This is nothing but a cloning fidelity, which can be shown to be equal to 5/6, i.e., the maximum value allowed by the no-cloning theorem. When attempting to increase the dimension of the qudit system to higher values, it is obviously critical to achieve with those systems the same level of control that has been already established for ordinary qubits, and the optimal cloning machine of OAM-carrying beams based on the Hong–Ou–Mandel effect was a striking demonstration of how much the simplicity of use provided by *q*-plates in handling OAM states can be beneficial to achieve this sort of result [28].

The *q*-plate can find also other uses in the field of quantum information technology. An interesting example is given by the property of those SAM + OAM states with vanishing total angular momentum to be invariant upon rotation [32].
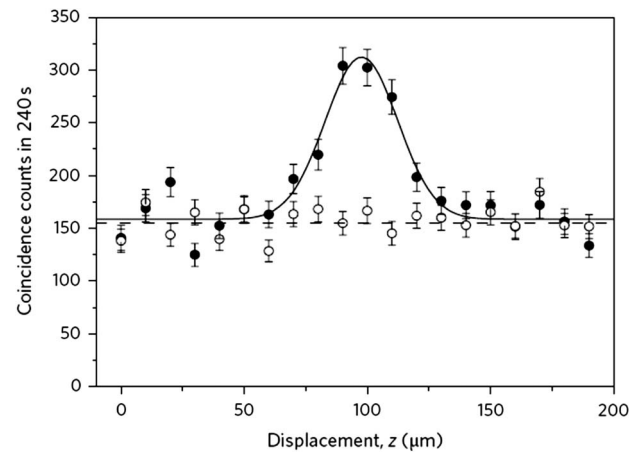

Fig. 6. Number of counts on the beam-splitter output as a function of beam displacement *z*, which is related to photon synchronization. For OAM-indistinguishable photons (solid circles) the Hong–Ou–Mandel effect takes place, as seen by increased number of counts, while for OAM-distinguishable ones (empty circles), there is no significant effect (reprinted with permission from Ref. [28]).

This property can be exploited in quantum communication, since the standard polarization encoding is prone to angular misalignment between the emitter and receiver reference frames [Fig. 7(a)]. By means of the spatial degree of freedom and due to the *q*-plate single-beam geometry, it is possible to encode the information in a rotation-invariant mode, which will not suffer any change in the relative angle between emitter and receiver, as basically both the SAM and the OAM parts will be affected in identical and opposite ways, compensating all rotation-induced phases. These proof-of-principle achievements were followed two years later by another work [33], in which a full quantum key distribution protocol was implemented with rotation-invariant OAM beams on a length-scale of hundreds of meters. The initial encoding and final decoding of information in the protocol can be conveniently performed in polarization space (and with optical fibers), while free-space transmission is done in the rotation-invariant hybrid SAM – OAM space. In Ref. [34], a quantum key distribution (QKD) with single photons has been realized with high-dimensional states in a turbulent free-space link of 0.3 km. The control of the radial profile of these complex SAM – OAM photonic states gives the opportunity to demonstrate hybrid high-dimensional QKD through obstacles with self-reconstructing single photons [35]. In free-space links, the effects of turbulence on the SAM – OAM classical entanglement of classical laser light have been used to characterize the perturbations on twin photons that are entangled in their OAM degree of freedom, providing an analysis of quantum channels by means of classical light in real time [36].

If one reverses the point of view, and poses the problem of how to measure precisely the angle between emitter and receiver, the extreme sensitivity of OAM values with large total angular momentum quantum number *m* can be of precious help. Polarization photonic gears are *q*-plate-based devices for achieving very sensitive measurements of angles. The principle works as follows: in order to measure an angle between
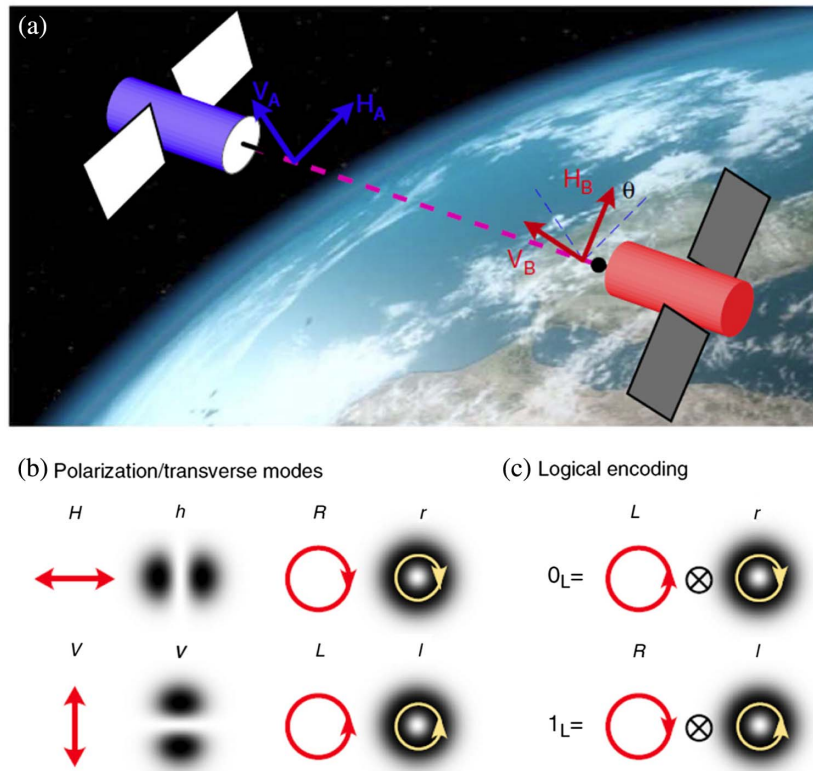
Fig. 7.   Emitter and receiver of a quantum message encoded with standard photon polarization must share good knowledge of the relative angle of each reference frame (a). Conversely, by combining polarization and transverse modes (b), it is possible to build two rotation-invariant (vanishing total angular momentum) orthogonal states (c), which can be used for rotation-invariant quantum communication (reprinted with permission from Ref. [32]).

emitter and receiver with linear polarization, one can imagine to write the electric field as a combination of left and right circular polarizations. Each component is rotated with respect to the receiver frame by an angle θ that is then measured. If one makes use of OAM beams with large total (SAM + OAM) angular momentum m, the relative phase of the two beams in the left/right base will now be $m\theta$, as the azimuthal angle in the expression of the OAM beam is multiplied by m. The receiver will thus measure an angle $m\theta$ instead of θ, thus realizing a large enhancement of its precision. This method has been proven by a q-plate with $q = 50$ so as to achieve a two orders of magnitude increase in angle measurement precision ($m = 2q + s = 101$) [37].

C. Simulating Quantum Walk Dynamics with OAM Beams

Q-plates are typically used to generate or characterize complex photonic states. However, they can play an invaluable role in the context of photonic simulations of quantum dynamics. Diverse optical setups have been developed in recent years to mimic the evolution of quantum particles (such as electrons) on discrete lattices. Lattice positions are encoded into non-overlapping optical modes (spatial, temporal, etc...), and among these modes, one could think of using beams carrying OAM. q-plates can be conveniently used to introduce couplings between neighboring modes [38,39]. In this scenario,

in recent years, particular attention has been paid to quantum walks [40–44]. A one-dimensional quantum walk can be seen as the time-evolution of a system (for instance, a particle, or in general, a "walker"). This evolution is one-dimensional if the space of walker states has a unitary dimension, and it is quantum if the internal two-state system, which determines the next n_{th} step (or "coin"), is a quantum state, unlike what happens in classical random walks, where the coin is a classical two-state system. The reason quantum walks have recently attracted so much attention from the research community is that they provide an ideal test-bed for understanding more complex quantum systems. For instance, they can be used as a playground for quantum simulation of topological phenomena. Topological phases in natural systems, such as topological insulators [45], are intriguing and novel emerging states of matter, and yet their intrinsic complexity makes their investigation difficult. The possibility to represent them with artificial systems that retain enough of the complexity to be suitable for the purpose, but also have enough simplicity to be realized and studied in detail, is therefore highly desirable. Photonic quantum walks seem to posses this property, as demonstrated, for instance, by the direct experimental demonstration of topologically protected bound states [46]. Q-plates can be useful in this context, as they provide for a simple and straightforward method for coupling the walker and the coin [47]. The set of all OAM states of the beam forms the walker one-dimensional infinite lattice system, and
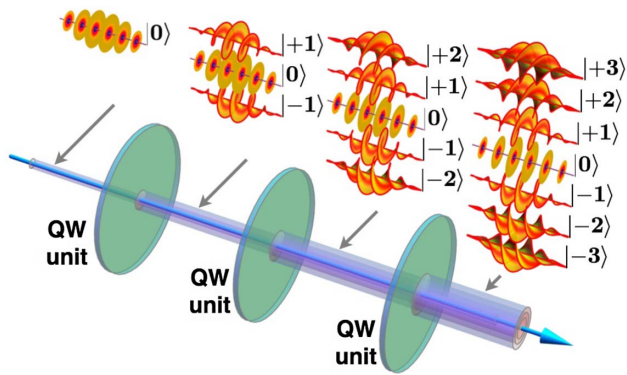
Fig. 8. Schematic representation of the quantum walk setup in which OAM modes are used to encode the walker position on the lattice. *Q*-plates are exploited to introduce the suitable quantum walk dynamics (reprinted with permission from Ref. [39]).

the circular polarization is the coin two-state (left and right) system. In this protocol, time is a discrete variable (steps), and each step is one passage into a pair of optics made by a quarter-wave plate for rotating the polarization (coin toss) and a *q*-plate for state transition (walker movement). Again, here the advantage of using *q*-plates instead of other mechanisms is twofold: on one hand, the coupling between SAM and OAM (which is not present in other OAM devices) and on the other hand, the simplicity of the *q*-plate operation geometry, which enables using a single-beam experimental setup with a fairly large number of steps, i.e., SAM – OAM interactions. A conceptual sketch of the quantum walk setup is shown in Fig. 8. Such a setup was first presented in Ref. [39], where a five-step quantum walk was demonstrated. Relying on the same platform, it has been possible to show that, by tuning the control parameter δ, one can actually realize quantum evolutions that are topologically non-equivalent [48]. In particular, abrupt variations in physical observables have been detected at transition points [49], and a nice, simple method to read-out the system's topological invariants has been devised and demonstrated experimentally [50]. Very recently, in Ref. [51], D'Errico and coworkers reported the realization of a novel setup, in which the walker degree of freedom is encoded in the 2D transverse wavevector of a paraxial beam. Here, to provide suitable quantum walk dynamics, LC gratings (named "g-plates" by the authors) replace the *q*-plates. This new setup has the intrinsic advantage of allowing for quantum-walk simulations over two-dimensional lattices.

4. BEYOND SAM – OAM CONVERSION: VECTOR BEAMS

The applications of *q*-plates in the first years were naturally devoted mostly to SAM – OAM conversion. However, the *q*-plate can operate in non-standard ways that open the route for more complex and exotic light structures. For example, in recent years, vector–vortex beams and polarization-singular beams have been generated by means of *q*-plates [52–54]. These peculiar beams possess nonuniform transverse polarization patterns, which are of interest in singular optics, such as, for instance, laser material processing [55], particle acceleration [56], optical trapping [57], and microscopy [58]. Some vector beam

examples are shown in Fig. 9. If one operates, indeed, the *q*-plate with a non-circular polarization input light beam (and properly adjusts the electric tuning), one can obtain a plethora of superpositions of different OAM states and polarization, which fall collectively under the name of vector beams.

Let us consider as an example the very simple case of linear horizontal polarization going through a perfectly tuned *q*-plate having $q = 1/2$. According to Eq. (2), the $|H\rangle$ state (where the horizontal/vertical directions are defined relative to the *q*-plate reference axis), which is a superposition of $|L\rangle$ and $|R\rangle$ states, will be converted into again a superposition of $|L\rangle$ and $|R\rangle$ states, i.e., a linear polarization, but whose relative phase now depends on the azimuthal angle ϕ. The resulting beam will thus be linearly polarized everywhere, but with its linear polarization pointing always towards the center of the beam. This vector beam is known as radially polarized. Similarly, by using a $|V\rangle$ input state, we can obtain a vector beam in which the polarization is normal to the radius in every point (azimuthal beams). These two examples are shown in Figs. 9(a) and 9(b). More complex and exotic structures have been generated by exploiting the electric tuning, as shown in Fig. 9(c) for $|L\rangle$ input state and $\delta = \pi/2$ phase retardation in the case of $q = 1/2$ ("lemon" beam), $q = -1/2$ ("star" beam), and $q = 1$ ("spiral" beam). Vector beams have a wide range of applications in optical tweezers [59], particle acceleration [60] and trapping [61], sharper focusing [13,62], improved laser cutting and drilling [63], enhanced microscopy [64], and metrology [37].

Beyond their applications in classical optics, vector beams have also been exploited to investigate quantum mechanics. They represent a novel resource in quantum information protocols, and their use triggered a large number of seminal demonstrations. Symmetric pairs of vector beams define two-dimensional spaces of non-uniform polarization states formally
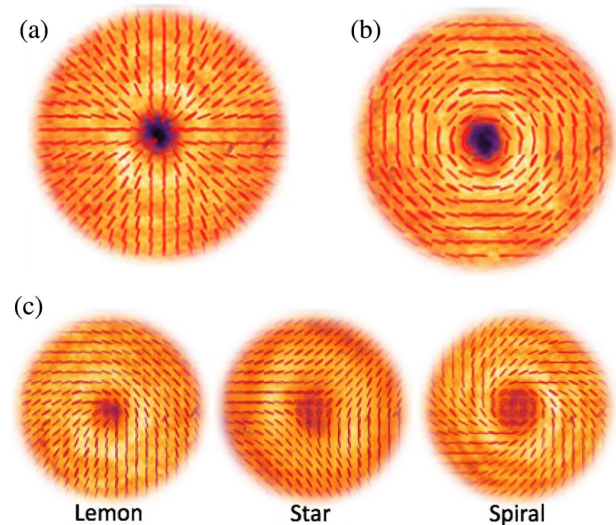
Fig. 9. Polarization topological structure generated by a *q*-plate with $q = 1/2$ and $\delta = \pi$ for H-linear (a) and V-linear (b) input polarizations (adapted from Ref. [52]). (c) Polarization-singular beams obtained when shining a *q*-plate with $\delta = \pi/2$ and $q = 1/2$ (lemon and star) and $q = 1$ (spiral); see Ref. [53]. The colormap brightness represents experimental beam intensity; the reconstructed experimental local polarization state is represented with small polarization ellipses.

analogous to the standard Poincaré sphere, which are known as hybrid Poincaré spheres or higher-order Poincaré spheres. Indeed, such beams correspond to states living in a high-dimensional hybrid SAM + OAM Hilbert space. Since the input light circular polarization sign determines the handedness of the induced OAM state, a classical superposition of polarizations (easily prepared with conventional optics) can be converted into quantum superpositions of positive and negative OAM values. A quantum superposition such as this naturally defines a qubit, but having the advantage of living (in principle) in an infinite dimensional space (a qudit). Finally, these states have been used to test the Hardy's paradox [65] and to investigate experimentally the violation of inequalities based on quantum contextuality [66].

In the following subsections, we will review a number of experiments in which the simple scheme briefly presented here, and originally demonstrated in Ref. [52], to generate vector beams has been replicated, in both quantum and classical regimes.

A. Laser Source Generating Complex Vector Beams

When dealing with vortex beams and other non-trivial light fields, one intriguing possibility comes to mind very naturally: a vortex laser, i.e., a laser source that can generate complex output modes instead of standard Gaussian modes in the first place, with controllable phase and polarization patterns on demand. The advantage is evident. A vortex laser would emit one single and clean higher-order spatial mode on request, such as, for instance, a Laguerre–Gauss mode, depending on the features of the laser cavity. When directly shining a q-plate or a spiral phase plate with a Gaussian beam, the output mode carrying OAM instead has a specific spatial structure, given by the so-called hyper-geometric Gaussian modes [67]. Furthermore, better efficiency can be achieved inside an optical cavity. In this case too, as in previously mentioned studies, the possibility to couple SAM and OAM offered by the q-plates,

together with their alignment-robust transmission geometry, was the key to open a new door. Q-plates allowed Naidoo and coworkers [68] in 2016 to build the first configurable vortex laser. One important reason that previous attempts to create such lasers failed is the degeneracy in the handedness of the azimuthal modes. The problem is that standard laser cavities do not distinguish modes $+l$ and $-l$, because their spatial intensity distribution is identical: same radii of curvature of the wavefront, same Gouy phase shifts. Therefore intracavity losses cannot be used for discriminating the two modes, and thus uncontrolled helicities are generated and amplified inside the cavity. Here, the q-plate can play an important role, because if the OAM state is difficult to control, the SAM degree of freedom is not. Therefore, SAM can be used to control OAM through the q-plate. A conceptual sketch of the laser cavity is shown in Fig. 10. The idea works as follows: a sequence of a quarter-wave plate and a q-plate forms a single SAM – OAM coupler module. Two modules are coupled in turn by a mirror (FM) that inverts the phase of both SAM and OAM components. If the waveplate and the q-plate are oriented along azimuthal angles β and γ (essentially equivalent to the α_0 angle, used in the notation in Section 2), respectively, then the second coupler will be oriented along $-\beta$ and $-\gamma$ for perfectly compensating the first one. Let us assume as an example that $|\beta| = \pi/4$, then each module will couple a homogeneous circular polarization state to a pure OAM state for any arbitrary value of γ, and a pure OAM mode with $+l = 2q$ will appear at the laser output. Similarly, linear vector beams can be created by properly adjusting the two angles of each module; for instance, a radial beam is created for ($\beta = 0$; $\gamma = 0$), and an azimuthal beam is created for ($\beta = 0$; $\gamma = \pi/2$), because the q-plates will work with linear polarization input, as already described at the beginning of Section 3. In actual laser realization, the two SAM – OAM coupler modules physically coincided, as the laser-cavity geometry was a V-shaped cavity
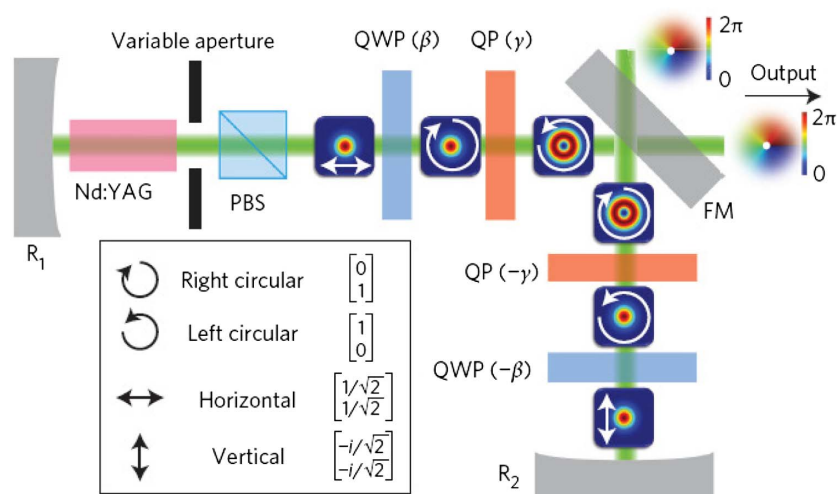
Fig. 10. Concept of the laser cavity for producing vector beams: Nd:YAG, active crystal; R1,2, end mirrors of the cavity; PBS, polarizing beam splitter; FM, polarization-insensitive out-coupling mirror; QWPs quarter-wave plates; QPs, q-plates (the angles in Greek letters correspond to the optical axis orientation for each optics). The pictures in the blue field show a colormap of the intensity pattern at each branch of the cavity. White arrows represent the polarization state according to the legend. In the actual V-shaped cavity, the two cavity branches were exploiting the same optical components with a small angular difference in the beam path (reprinted with permission Ref. [68]).

with a few-degree angular aperture, so that light reflected at the FM passed through part of the same cavity optics. With these methods, the authors were able to generate any possible vector beam with mode purity (i.e., the ratio of the power of the desired mode with respect to the total optical output power) as high as 98%.

B. Classical Communication with Vector Beams

The spatially inhomogeneous polarization of vector beams can be used to increase the transmission data rate of free-space optical communication by mode division multiplexing. The q-plates in this case can be used as mode (de-)multiplexers for vector modes, in a fashion similar to what was already described in Section 3.A. As a proof of principle, four vector modes, each carrying a 20-Gbit/s quadrature phase shift keying signal, for a total rate of 80 Gbit/s, on a single wavelength channel ($\lambda \sim 1550$ nm) were transmitted on a single meter distance in the laboratory with less than 16.4 dB mode cros-talk. A major challenge for using mode multiplexing in free-space optical communication is atmospheric turbulence [69]. With respect to this issue, numerical simulations show that vector beams should have an advantage over OAM beams, because a vector mode could experience less scintillation upon propagation through atmospheric turbulence as compared to a pure OAM mode [70]. The radially dependent amplitudes of vector modes and OAM modes are expected to be comparable, and it is anticipated that the divergence of vector modes as they propagate through atmospheric turbulence is comparable to that of OAM modes. These simulations have not been confirmed experimentally yet. Nevertheless, the deleterious effects of atmospheric turbulence can be compensated via the measurement of spatially inhomogeneous polarization [71], using a similar approach to that used for compensating the OAM modes alteration in free-space propagation via wavefront measurements [72]. Going beyond free-space communication, the use of vector beams and q-plates as (de-)multiplexers could also be beneficial for optical-fiber communication [73], since vector modes are close to the "true modes" of optical fibers [74].

C. Quantum Information with Vector Beams

For communication, either classical or quantum, the ability to store information is a crucial keystone. However, while storing classical information is relatively easy, and it is routinely done in many devices already available today, quantum information requires storing of quantum phases, which are much more fragile and hard to preserve. In this respect, the work by Parigi and coworkers [75] represents a significant advance in this research field. The storage and subsequent retrieval of information encoded with vector beams—at the single-photon level—has been achieved using a multiplexed ensemble of laser-cooled cesium atoms, prepared inside a magneto-optical trap (see Fig. 11). This setting requires simultaneous reversible mapping of polarization and spatial degrees of freedom, which is a nontrivial capability. In this experiment, a set of vortex beams is generated by q-plates and mapped into and out of the memory cells dynamically. The rotational invariance of the vector beams is preserved in this procedure, with fidelities close to unity and exceeding classical benchmarks for memory protocols. The protocol works on a three-level system, namely, two hyperfine ground states $|g\rangle$ and $|s\rangle$ and one excited state $|e\rangle$ (upper-left panel in Fig. 11). The light to be stored addresses the $|g\rangle$ – $|e\rangle$ transition. A control beam on the $|s\rangle$ – $|e\rangle$ transition is first shined on the atomic ensemble. By switching off this beam, the optical states are then coherently mapped onto a collective material spin excitation. Switching on the control beam at a later time (in µs scale, lower-left panel in Fig. 11) triggers light emission and allows retrieval of the signal, at the single-photon level, in the same spatial mode, due to a collective enhancement effect.

For real-life quantum information protocols to be achieved, not only storage is important. One of the biggest challenges in this field is of course to minimize disturbances that can affect the message along its journey. Spatial properties of light are severely affected by spatial perturbations, such as the optical turbulence present in the atmosphere. Since hybrid qubits exploit OAM properties, they are also susceptible to atmospheric turbulence. This raises the question of whether the use of this
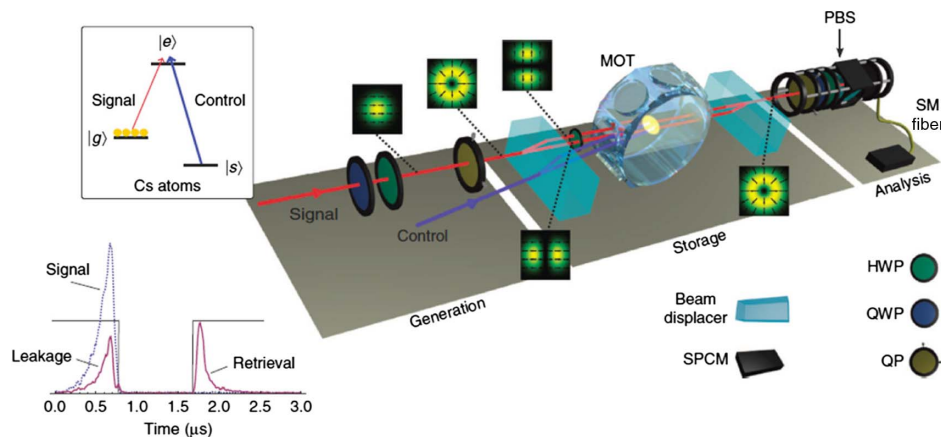
Fig. 11. Experimental scheme for the vortex beam quantum memory. QP, q-plate; HWP and QWP, half- and quarter-wave plates, respectively; PBS, polarizing beam splitter; SM fiber, single-mode fiber, SPCM, single-photon counting module; MOT, magnetic optical trap where the information is stored in a cold atoms ensemble. The levels diagram (a) and delayed retrieval of the signal (b) are shown in the insets (reprinted with permission from Ref. [75]).

additional degree of freedom does indeed provide a practical advantage. Even if OAM optical systems encoding classical information have recently started to be tested in real scenarios over distances on the order of kilometers with positive results [76], future technologies for the transmission of quantum information must prove themselves to be more robust. So far, this was proven to be feasible, at least in the weak turbulence regime. In this intermediate regime a transmission fidelity close to unity was achieved for rotational invariant qubits [32,77]. This robustness is due mainly to logical encoding and decoding procedures, both based on q-plates. Spatial perturbations with mirror symmetry in the OAM space result only in signal losses, rather than qubit state errors. The idea works according to this line: qubits are prepared with anti-symmetric OAM eigenstates $|l\rangle$ and $|-l\rangle$. The two wave functions are equivalent under mirror reflection, so spatial perturbation with this symmetry affects both components equally. In the decoding procedure, the projection onto a zero-order OAM mode transfers the encoded information to the polarization degree of freedom, so that the effects of the OAM perturbation factor out, as they affect both OAM states equally. Of course, arbitrary turbulences do not have specific mirror symmetry, but it can be shown that in the weak turbulence regime, the perturbation appears as a multiplicative spatially dependent phase term, and this is enough to guarantee mirror symmetry. More refined protocols will be necessary to access the strong turbulence regime.

Another very interesting application of the q-plate in the quantum regime is the entanglement of vector–vortex beams. As known, the entanglement is a key concept in modern physics and one of the most enigmatic demonstrations of the quantum laws in nature. For entangled photons, however, the interest in fundamental physics is combined with a very applicative interest in quantum information technology. Entangled photons have been used for instance to demonstrate the first example of teleportation [29] and Bell's inequalities test [78]. The entanglement of photons can affect different degrees of freedom, such as frequency or path, and of course OAM and polarization. As vector–vortex beams are non-separable superpositions of SAM and OAM eigenmodes, photons in a vector beam are actually entangled "with themselves" on these two degrees of freedom (also called intra-system entanglement). On one hand, this single-particle entanglement cannot be used, of course, for proving non-locality, as it regards a single particle in a single spatial region. On the other hand, when preparing a pair of entangled photons in a vector–vortex spatial mode, a two-particle entanglement (similar to what was done in several other experiments on the SAM states alone) can be realized, as shown by D'Ambrosio and coworkers in 2016 [79]. The authors showed that both the intra-system entanglement between each photon SAM and OAM states and the inter-system entanglement between the two photon states are obtained at the same time. The former is related to the structure of vortex states, and the latter corresponds to entanglement between two complex vectorial fields. By performing a non-locality test in the vector–vortex space, it was shown that entanglement between complex vectorial fields can be effectively exploited as a resource in fundamental quantum mechanics as well as quantum information. The key element for producing such

entangled states was the q-plate, as its use enabled the possibility to convert a usual two-photon polarization-entangled state obtained by nonlinear frequency conversion scheme to a SAM + OAM entangled two-photon state. The q-plates are also very useful not only just for creating a given (and simple) vector beam, such as radial or azimuthal beams, but also for manipulating the beam in a very controlled and programmable fashion. The electrical manipulation of vector–vortex beams to obtain transformations describing curves entirely contained on a given hybrid Poincaré sphere is quite challenging, as it requires simultaneous action on both polarization and OAM degrees of freedom. But due to this electrically tunable device, any arbitrary transformation on the Poincaré sphere can be obtained, with high fidelity [80].

5. STRUCTURING LIGHT TO STRUCTURE MATTER

When light interacts with condensed matter, the geometrical shape of the material inside the interacting region is not significantly affected to first approximation. The simplest thing that can happen is the absorption of one photon by one atom or molecule, which changes the internal state of the particle only until the energy relaxation restores the system to the ground state, releasing some heat. A photon may change the molecular shape as well, as, for instance, in cis-trans photoinduced transitions, but not the molecule position in space. When the interaction is very intense, however, more dramatic changes may take place. In this case, the simplest example we can think of is a thermally induced phase transition. In this case, the light acts mainly as a heat source. In fact, even in more complex phenomena, the interaction follows predominantly the intensity pattern of the light beam. There are cases, though, where this is not true, in the sense that the intensity pattern alone cannot explain the symmetry of the shapes transferred—or written—into the surface, either transiently or permanently, and the vectorial or phase structure of the illuminating field plays a role. In the following two subsections, we will analyze some interesting examples that have been obtained in soft and solid-state matter. In the case of soft matter, the vortex beams have been achieved by means of SLM and not by q-plates, but these results have been included here for completeness.

A. Soft Matter

Azobenzene is a chemical compound composed of two phenyl rings linked by a N=N double bond, and it undergoes photoisomerization of trans- and cis-isomers. The two isomers can be switched with light at particular wavelengths: usually blue/ultraviolet for trans-to-cis and green/blue for cis-to-trans isomerization. The process occurs in the picosecond time scale, while the subsequent relaxation is much slower, depending on the specific compound, and it can reach several hours. As the direction of the two rings connected by the N-bond defines a natural axis of the molecule, oriented molecules display non-isotropic properties, such as optical birefringence. The orientation can be induced by light itself, because the trans-molecules tend not to absorb photons with a polarization perpendicular to the molecule axis, and therefore a prolonged illumination with linearly polarized light will increase the amount of

trans-molecules oriented in the direction perpendicular with respect to light polarization [81]. However, light can change not only the orientation of the azobenzene molecules, but also their position in space, a phenomenon known as light-induced mass migration. It can thus reshape the surface of a thin film [82] and induce the formation of a stable patterned surface, whose structures are permanent and can be erased by heat or by illuminating with incoherent uniform light. Obviously, these findings may have a potential impact, e.g., for optical data storage applications. Most widely accepted models for explaining this peculiar behavior are based on intensity gradients and polarization, as these are the two main ingredients that play a role in the mass migration. Therefore, two vector–vortex beams with opposite handedness but identical topological charge and polarization patterns should result in identical patterns on the surface, because their intensity and polarization profiles are identical. It turns out, by the pioneering work of Ambrosio and coworkers [83], that this is not the case. Figure 12 shows two atomic force microscopy images of the surface of an azo-polymer thin film illuminated with two vector–vortex beams having linear polarization everywhere but opposite handedness corresponding to $m = \pm 10$, respectively. It is evident that the polymer responds not only to the intensity and polarization distribution of the light field but also to its phase, i.e., to the helical wavefront shape. The authors proposed a semi-empirical model based on symmetry considerations: the phase of the vortex beam can play a dominant role in the writing process if an interference between the transverse optical field components E_x and E_y and the longitudinal component E_z is allowed. This is not the case in isotropic media, but it is possible in azo-polymers 2D surfaces, due to the anisotropic response of the material, which breaks the rotational symmetry. This phenomenological model was extended to a full microscopic model one year later [84].

B. Condensed Matter

While in azo-polymers, the interaction with light is mediated by resonant transitions and the anisotropic properties of the material, other effects of that sort can be produced even on much simpler elements, such as, e.g., silicon, and many other semiconductors or dielectrics. The point in that case is not
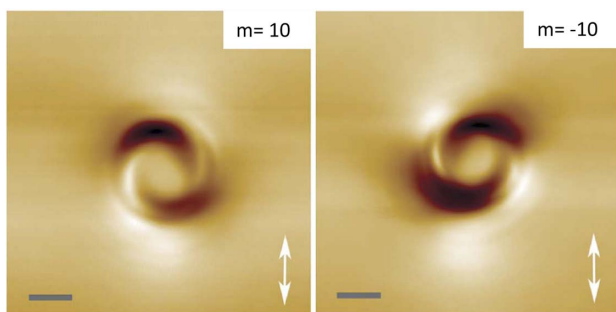
Fig. 12. Spirals with opposite handedness revealed by atomic force microscopy can be written on azo-polymer surfaces by means of two opposite handedness vortex beams with $m = +10$ (left panel) and $m = -10$ (right panel). White arrows indicate the linear polarization of the beams. Scale bars represent the length of 1 µm (reprinted with permission from Ref. [83]).

much about the material response itself, but about the response of hot and dense plasma, which is formed when the material is irradiated violently with an intense laser pulse. All these sometimes simpler and sometimes very complex effects go collectively under the name of "laser ablation." Ablation by laser pulses is a quite widely used technique for different purposes. To cite a few among others, one can mention pulsed-laser deposition [85], in which the elements of the target material are ablated by a laser pulse and then condensed back into a crystalline form on top of a substrate surface to realize thin films with single atomic layer control, or surface micro- and nano-structuring [86] with a plethora of different applications, from adhesive and friction enhancement to coloring and aesthetic finishing.

When using ultra-short pulses (in the femtosecond regime) for laser ablation, the available time for interaction between the plasma and electromagnetic field of light is much shorter compared to more standard nano- and picosecond pulse durations. As a consequence, the main light–matter coupling occurs via multiphoton excitation of electrons into the conduction band or the vacuum (assumed to be instantaneous). The laser impact results thus in the emission of a considerable amount of electrons, leaving behind positive holes in the surface region. The time for bulk electrons to fill these holes is on the order of picoseconds, and therefore the region will be positively charged for a considerable amount of time and becomes electrostatically unstable. As a consequence, the surface will break apart by emitting positive particles (ions or clusters), which will be accelerated in the residual field. This electrostatic repulsion catastrophe is known with the name of "Coulomb explosion." The lattice destabilization has other consequences too: it relaxes via self-organized formation of regular micro- and nanostructures at the irradiated area, with a strong influence of laser polarization on structural symmetry, which is still not completely understood. One example is the formation of ripples, linear structures made of parallel lines, with a sub-wavelength period and direction that depends on beam polarization. Moreover, secondary effects can take place, such as the decoration of the irradiated area with nano-particles, attached to the surface after their formation outside the material, in the ablation plume [87].

Q-plates have been used quite extensively in the last four years to produce both pure OAM beams and vector–vortex beams to be used for laser ablation of metals and semiconductors. Amoruso and coworkers [88–95] have shown a variety of novel and interesting effects connected to the contemporary presence of structured wavefronts and ultra-short pulses. The central part of the ablated area (which corresponds to the hole of the doughnut, the singular point with vanishing intensity) is not affected by ablation, as one could expect, but only for low values of irradiation and number of shots. At higher values of these two parameters, the hole starts to host most of the nanoparticles created by ablation in the surrounding area, so much that it will eventually fill up and form a central 3D structure that resembles a pillar made of nanoparticles [89]. Ripples have been observed as well, with size and shape that depend on the fluence and number of shots, whose direction is orthogonal to local laser polarization, as already observed

with non-structured light. In addition, novel unexpected features appear. Figure 13 shows the ablation pattern obtained on (100)-silicon using different vector beams (represented in the top left corner). The ripples with orthogonal direction are seen on the outer and inner parts of the ring, where the laser fluence is low. But in a large central annular region with high laser fluence, the structures are much larger (and thus they took another name: "grooves") and oriented parallel to beam polarization. For all investigated vector beams, grooves aligned parallel to the local beam polarization are present in the high-fluence region, while ripples perpendicular to polarization are formed in the low-fluence areas.

Detailed investigations of the dependence of the two external and internal radii of ablated surface as a function of both laser fluence per pulse and total number of pulses revealed [90] that a specific single-shot threshold fluence $F_{\text{th},1}$ exists and that the threshold fluence for N pulses is given by the relationship $F_{\text{th},N} = F_{\text{th},1} N^{\xi-1}$, where ξ is a material-dependent incubation factor (which was found to be 0.81, consistent with previous results for non-structured light on silicon [96]). The reason that the threshold fluence decreases with N can be understood quite simply if we consider that a pre-formed deformation or damage at the $(N-1)^{\text{th}}$ pulse determines a stronger effect of the Nth pulse because of defect-assisted absorption or other more complex mechanisms, which take the collective name of "incubation effects." This was already known for ripples, but not for grooves, whose formation follows exactly the same incubation law with very similar factor (0.88) but higher single-shot threshold. Interestingly, one can analyze the pattern formed very close to the crossing between fluences below and above the ripples-to-grooves threshold, and find that the two structures are both visible and partially overlapped, suggesting a smooth transition rather than an abrupt change in the ablation processes. In particular, the similarity between the two incubation factors suggests that a common physical process is at play. A recent but relatively well-accepted model for the ripples formation is the Sipe–Drude theory [97], which accounts for the interaction between an incident plane wave and surface scattered waves caused by the material's surface roughness. Although Nivas and coworkers have shown that a revised version of this theory could account for some features relative to the grooves formation too, a more detailed and exhaustive model is still lacking.

The investigation of this multi-focus topic has continued in many directions: ablation on metal surfaces [88], the use of ablation patterns to characterize the Laguerre–Gauss vector beams [95], and the use of partially converted beams (or complex superpositions of OAM eigenstates) for generating non-standard shapes, which could be used, for instance, to create laser-ablated periodic sub-wavelength structures (meta-materials) [94].

## 6. FUNDAMENTAL RESEARCH ON COMPLEX STRUCTURED LIGHT

This section of the paper is devoted to describing those works—still performed with the use of q-plates or of other devices that represent q-plate generalizations—that concern neither the generation or control of OAM and SAM eigenstates nor the superposition of few such eigenstates, but whose aim is instead to study the fundamental physics of more complex structured light beams.

Perhaps the most prominent example of this kind of study is the work by Bauer and coworkers [13], where the formation of a very peculiar polarization structure in the focal plane of a highly non-paraxial vector beam has been observed. In 1975, it was pointed out [98] that longitudinal components of an electromagnetic field must exist for any solution of the Maxwell equations, except for linearly polarized plane waves. The longitudinal component can be, however, quite small and difficult to measure, except in proximity of a tight focus, where the paraxial approximation is no longer valid [99]. It is intriguing thus to investigate what sort of shape the field in the focal plane will take in the case of tight focusing of twisted light. The emergence of a non-negligible longitudinal component could somehow transfer the twist in three dimensions. And indeed, something like this happens, as the authors found that the spatial structure formed by the major axis of the 3D polarization ellipse is a Möbius strip.

The Möbius strip is a peculiar 2D surface that does not possess a well-defined orientation. That means one can go from the upper to the lower surface without crossing the border, or alternatively one can follow the left border and then arrive to the right side of the strip without moving across the surface. Therefore, there are no lower or upper surfaces, nor left or right borders. This kind of structure can be realized in many artificial ways, but it is remarkably difficult to find in nature. Here, the strip is formed by the plane described by light polarization. Let us refer to Fig. 14: the circular image on the left of each panel represents a standard intensity map of the beam in the focal plane, with color coding for light intensity and the plane of the figure coincident with the xy plane in the focus, z being the propagation direction. If we ideally draw a circle around the center of the beam (indicated with a dashed line, which corresponds to the red circle in the main images) and then measure the polarization ellipse of light at every point of that circle, we find that the angle of its major axis changes and turns around
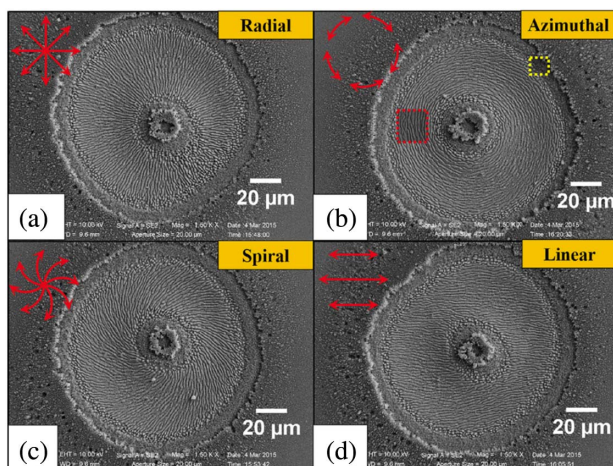
Fig. 13. SEM micrograph of the target silicon surface after laser irradiation (number of pulses $N = 100$, energy per pulse $E_0 = 48$ μJ) with different vector beams: (a) radial, (b) azimuthal, (c) spiral, and (d) linear. The red arrows in the upper left corner represent the polarization state (reprinted with permission from Ref. [90]).
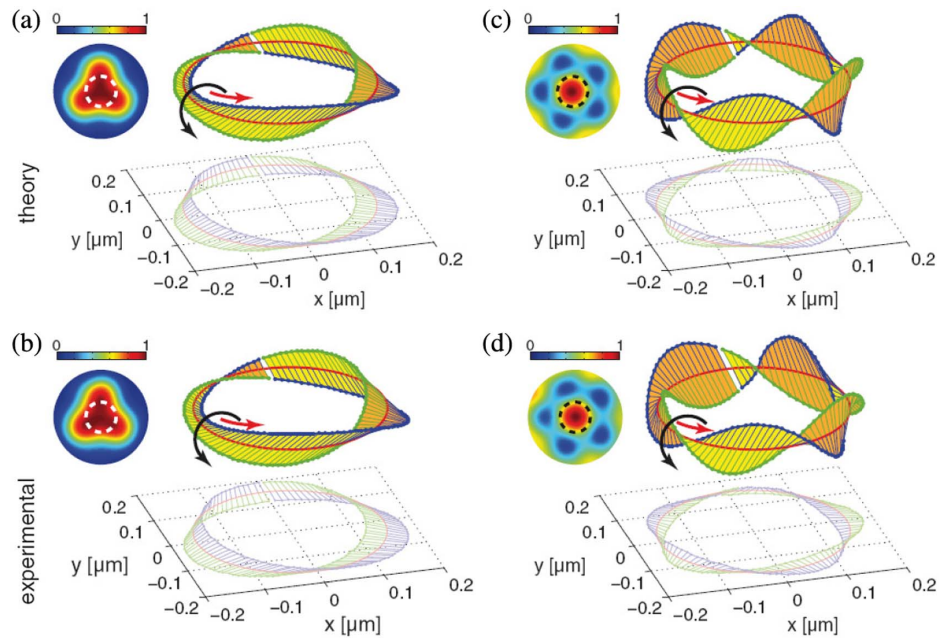
Fig. 14. Panels A and C show the expected polarization topologies in the focal plane of a highly non-paraxial vector beam with topological charges $q = -1/2$ and $q = -3/2$, respectively. Panels B and D show the experimentally observed polarization topologies. In all plots, the major axis of the 3D polarization ellipse is represented as a function of position on a circle of 150 nm radius centered on the beam axis (shown as a dashed white or black line in the top-left insets). The four insets show the beam intensity in the focal plane. One half of the major axis of the local polarization ellipse is colored blue, and the other half is colored green, in order to better follow the twists of the polarization vector (reprinted with permission from Ref. [13]).

the circle itself, several times, describing the Möbius strip, until it comes back to the same orientation when completing the round trip. This behavior is made more clearly visible in the figure by drawing one half of the polarization ellipse axis with green and the other half with blue, but this axis apparent polarity does not correspond to a physical property. Indeed, the polarization ellipse axis must not be confused with the instantaneous electric field (which is obviously polar).

This peculiar behavior has been observed experimentally with a technique based on a quite complex reconstruction of images taken with several masks of the light scattered from a nanoparticle placed in a given point of the beam where the electric field of light is to be measured [100]. The vector beams used in the experiment have been obtained with detuned q-plates, and are a superposition of the fundamental Gaussian and OAM$= \pm 2q$ modes with opposite circular polarizations. The symmetry of the obtained beam belongs to the class of star symmetry [see Fig. 9(c)], the topological charges investigated are $q = -1/2$ and $q = -3/2$, and the ratio between the two modes can be adjusted by varying the phase retardation δ using an applied voltage, as already described. Looking at Fig. 14, it is evident that the number of half-twists made by the ellipse major axis depends on the topological charge used for creating these vector beams.

Another work that deals with more foundational and general issues is reported in the paper by Piccirillo and others [101] about the measurement of OAM mean value and variance. When dealing with unknown superpositions of—in principle—infinite OAM eigenstates, the only way to measure the mean

value and variance of the eigenvalues distribution is to measure the OAM spectrum, i.e., to project the superposition on a very large number of states and measure each of the superposition coefficients. However, if one is interested in having only a synthesis of this large amount of information, as represented by the mean value and variance, one can take another route, related to the topic of weak measurement in quantum mechanics. The basic idea is to let a simple system interact with the target system weakly, which means not to drastically change it (as a standard projective measurement would do because of the wavefunction collapse). Once this pre-measurement is done, the state of the ancillary system is measured, and the mean values and variance of the target state are reconstructed. In the work by Piccirillo _et al._, the target state is represented by the OAM state of the beam, and the ancillary system by the SAM of the beam. For the sake of brevity, we will not discuss the details of the method here. What it is interesting to note in this review is the unusual mode of operation of the q-plate used in the experiment. The q-plate was employed to generate known OAM superpositions for calibrating the system and unknown (and very large) superpositions for testing the method. The former case was managed with usual control of the input circular polarization and plate voltage. The latter was obtained in a more exotic way, by using the q-plate in a off-axis mode. The test beam was generated by means of a perfectly tuned q-plate with $q = 4$, for circular polarization input, but the center of the beam was translated off the plate's central singularity by a variable distance x_{ms}. In this situation, the input beam in the measurement setup is similar to a Gaussian beam

with an added vortex located at a distance x_{ms} from the beam axis. This is not an eigenstate of OAM, but it is instead a superposition of many different values of the OAM quantum number l. This method has been validated for values of l up to 8.

The same method for producing large OAM superpositions was employed by D'Errico and coauthors [54] last year to measure the full OAM distribution of an arbitrary paraxial optical field by means of digital analysis of the interference pattern formed by the target OAM beam and a reference Gaussian beam. The method takes advantage of the possibility to measure images rather than integrated intensities. If one measures a total of four images, two corresponding to the target and reference beams alone and two corresponding to both beams having a relative optical phase retardation of 0 and $\pi/2$, it is possible—after suitable digital processing of the images—to reconstruct the full OAM power spectrum, also known as spiral spectrum. In this method, the largest OAM eigenvalue that can be measured depends mainly on the camera resolution.

A. Beyond *Q*-Plates: Geometrical-Phase Optics

So far we have reviewed different ways of using standard *q*-plates. However, we shall mention in this last subsection that *q*-plate technology, as already anticipated in Section 2, is capable of creating more complex spatial LC structures. The simplest thing that can be made when preparing a *q*-plate is to alter the computer-controlled movement of writing polarization and plate angles. Any relationship between the angle α of each molecular axis and the azimuthal coordinate ϕ can be programmed. For example, we consider the following structure:

$$\alpha(\phi) = q \tan^{-1}[a \tan(\phi + \gamma)] + \alpha_0. \tag{3}$$

This relationship defines an ellipse with ellipticity a rotated by an angle γ, so that these structures have been called elliptical *q*-plates, whereas the same relationship for $a = 1$ defines a circle and corresponds to the formula already presented in Section 2. This kind of special *q*-plate has been successfully utilized for creating "monstar" dislocations [102], i.e., topological polarization structures that are intermediate between a "lemon" and a "star" pattern, as already described in Fig. 9, and to obtain elliptical nodal areas in coherent light beams [103]. This last work could be very beneficial for astronomy in the emerging field of vortex-phase-mask coronagraphy [104,105].

Finally, when considering general orientation patterns that can be written by photo-alignment on the *q*-plate, we can get out of the vortex beam research field and back to a more old-fashioned topic in optics, i.e., lens fabrication [106]. A standard lens is essentially a device that bends the wavefront of a light beam, and it does so by spatial modulation of the optical path at different positions in the transverse plane of the beam. A very similar wavefront transformation, though, can be obtained by introducing suitable PB phases. This has been realized by letting the LC axis angle α be a function of both the azimuthal ϕ and the radial r coordinates. Such a lens is quite different from a usual one. First of all, it is flat and only a few micrometers thick (the thickness of the LC layer in between the glass plates); second, it can work in different modes for different polarizations, for instance, converging for left-circular input and diverging for the right one; and third, the phase retardation δ can be controlled by electric voltage, and therefore the lens

can be switched on and off on demand, or it can work for different colors, selectively, as we have already seen for *q*-plates in many applications. This concept was used last year to build a proof-of-principle discrete-elements example of a geometrical-phase waveguide [107]. Of course, by exploring even more complex arrangements of the LC molecules, many more kinds of geometrical-phase optical elements will be fabricated in the future: here the possibilities are limitless and largely unexplored.

7. CONCLUSION

From its introduction in 2006 until now, the *q*-plate device has found a surprising number of diverse applications. In this progress review, we have surveyed many of the most significant ones, focusing mainly on results reported in the last 5–7 years. Let us now briefly discuss what could be the future prospects of this technology, also in the more general framework of the field of structured light [108].

A first likely line of future development is towards more general 2D and even 3D control of optical fields. 3D here stands for involving all three orthogonal field components, as already demonstrated in pioneering works such as the polarization Möbius strip [13], but also for space-variant in all three spatial coordinates, as in 3D-structured optical pulses. We expect that suitable *q*-plate elements in combination with other kinds of optical technologies will be able to improve the control on obtained structured light, for example by better combining radial and azimuthal structuring [109], improving the spatial resolution [110], and push the boundary of achievable structures even further. This in turn may find applications in more advanced optical manipulation (optical tweezers), optical material processing, optical filtering and coronagraphy, or in light-matter space-time-modulated interaction a, for example for quantum simulations with atoms or ions.

Another interesting area of likely progress is the one combining *q*-plates, OAM modes and waveguides, or more generally integrated optics. Very recently, the first integrated waveguides carrying vortex modes have been demonstrated [111]. Multiple-mode waveguides could be used in the near future for optical processing with increased functionalities, particularly in the quantum domain. A research effort towards using few-mode fibers for mode-division multiplexing in optical communication is currently under way and *q*-plates have already played a crucial role in coupling such modes in and out of the fibers. This effort will likely continue and be pushed even further, by increasing the number of available modes and improving the overall performances in terms of cross-talk. If successful, this is one area in which the chances of getting into real-world applications are high. The recently demonstrated waveguiding principle based on geometrical phases [107,112,113] could soon be demonstrated in continuous systems and applications based on it are likely to emerge.

Q-plate technology is currently being extended to different wavelength ranges, such as far-infrared and THz-waves on one side [114,115], ultraviolet and possibly even x-rays on the other side. Finally, the arrangement of large numbers of *q*-plate devices in sequence or in transverse arrays, or both, may further expand the range of application possibilities, introducing

entirely new ways of controlling light propagation and evolution. The first examples of such devices are already promising in this sense [39,51,116,117].

REFERENCES

1. H. He, M. E. J. Friese, N. R. Heckenberg, and H. Rubinsztein-Dunlop, "Direct observation of transfer of angular momentum to absorptive particles from a laser beam with a phase singularity," Phys. Rev. Lett. **75**, 826–829 (1995).
2. A. T. O'Neil, I. MacVicar, L. Allen, and M. J. Padgett, "Intrinsic and extrinsic nature of the orbital angular momentum of a light beam," Phys. Rev. Lett. **88**, 053601 (2002).
3. A. Forbes, A. Dudley, and M. McLaren, "Creation and detection of optical modes with spatial light modulators," Adv. Opt. Photon. **8**, 200–227 (2016).
4. R. Bhandari, "Polarization of light and topological phases," Phys. Rep. **281**, 1–64 (1997).
5. G. Biener, A. Niv, V. Kleiner, and E. Hasman, "Formation of helical beams by use of Pancharatnam-Berry phase optical elements," Opt. Lett. **27**, 1875–1877 (2002).
6. L. Marrucci, C. Manzo, and D. Paparo, "Optical spin-to-orbital angular momentum conversion in inhomogeneous anisotropic media," Phys. Rev. Lett. **96**, 163905 (2006).
7. L. Marrucci, C. Manzo, and D. Paparo, "Pancharatnam-Berry phase optical elements for wavefront shaping in the visible domain: switchable helical modes generation," Appl. Phys. Lett. **88**, 221102 (2006).
8. F. Bouchard, H. Mand, M. Mirhosseini, E. Karimi, and R. W. Boyd, "Achromatic orbital angular momentum generator," New J. Phys. **16**, 123006 (2014).
9. E. Karimi, S. A. Schulz, I. De Leon, H. Qassim, J. Upham, and R. W. Boyd, "Generating optical orbital angular momentum at visible wavelengths using a plasmonic metasurface," Light: Sci. Appl. **3**, e167 (2014).
10. R. C. Devlin, A. Ambrosio, N. A. Rubin, J. P. B. Mueller, and F. Capasso, "Arbitrary spin-to-orbital angular momentum conversion of light," Science **5392**, eaao5392 (2017).
11. G. Vallone, G. Parisi, F. Spinello, E. Mari, F. Tamburini, and P. Villoresi, "General theorem on the divergence of vortex beams," Phys. Rev. A **94**, 222–225 (2016).
12. M. Erhard, R. Fickler, M. Krenn, and A. Zeilinger, "Twisted photons: new quantum perspectives in high dimensions," Light: Sci. Appl. **7**, 17146 (2018).
13. T. Bauer, P. Banzer, E. Karimi, S. Orlov, A. Rubano, L. Marrucci, E. Santamato, R. Boyd, and G. Leuchs, "Observation of optical polarization mobius strips," Science **347**, 964–966 (2015).
14. F. Kong, C. Zhang, F. Bouchard, Z. Li, G. G. Brown, D. H. Ko, T. J. Hammond, L. Arissian, R. W. Boyd, E. Karimi, and P. B. Corkum, "Controlling the orbital angular momentum of high harmonic vortices," Nat. Commun. **8**, 14970 (2017).
15. S. Slussarenko, A. Murauski, T. Du, V. Chigrinov, L. Marrucci, and E. Santamato, "Tunable liquid crystal q-plates with arbitrary topological charge," Opt. Express **19**, 4085–4090 (2011).
16. B. Piccirillo, V. D'Ambrosio, S. Slussarenko, L. Marrucci, and E. Santamato, "Photon spin-to-orbital angular momentum conversion via an electrically tunable q-plate," Appl. Phys. Lett. **97**, 241104 (2010).
17. S. Slussarenko, B. Piccirillo, V. Chigrinov, L. Marrucci, and E. Santamato, "Liquid crystal spatial-mode converters for the orbital angular momentum of light," J. Opt. **15**, 025406 (2013).
18. L. Marrucci, "The q-plate and its future," J. Nanophoton. **7**, 078598 (2013).
19. L. Yan, P. Gregg, E. Karimi, A. Rubano, L. Marrucci, R. Boyd, and S. Ramachandran, "Q-plate enabled spectrally diverse orbital-angular-momentum conversion for stimulated emission depletion microscopy," Optica **2**, 900–903 (2015).
20. Y. Rumala, G. Milione, T. Nguyen, S. Pratavieira, Z. Hossain, D. Nolan, S. Slussarenko, E. Karimi, L. Marrucci, and R. Alfano, "Tunable supercontinuum light vector vortex beam generator using a q-plate," Opt. Lett. **38**, 5083–5086 (2013).
21. E. Karimi, L. Marrucci, C. De Lisio, and E. Santamato, "Time-division multiplexing of the orbital angular momentum of light," Opt. Lett. **37**, 127–129 (2012).
22. P. Gregg, M. Mirhosseini, A. Rubano, L. Marrucci, E. Karimi, R. W. Boyd, and S. Ramachandran, "Q-plates as higher order polarization controllers for orbital angular momentum modes of fiber," Opt. Lett. **40**, 1729–1732 (2015).
23. K. Ingerslev, P. Gregg, M. Galili, F. Da Ros, H. Hu, F. Bao, M. Usuga Castaneda, P. Kristensen, A. Rubano, L. Marrucci, K. Rottwitt, T. Morioka, S. Ramachandran, and L. Oxenlowe, "12 mode, WDM, mimo-free orbital angular momentum transmission," Opt. Express **26**, 20225 (2018).
24. G. Tosi, F. Marchetti, D. Sanvitto, C. Antón, M. Szymańska, A. Berceanu, C. Tejedor, L. Marrucci, A. Lematre, J. Bloch, and L. Viña, "Onset and dynamics of vortex-antivortex pairs in polariton optical parametric oscillator superfluids," Phys. Rev. Lett. **107**, 036401 (2011).
25. L. Dominici, G. Dagvadorj, J. Fellows, D. Ballarini, M. De Giorgi, F. Marchetti, B. Piccirillo, L. Marrucci, A. Bramati, G. Gigli, M. Szymańska, and D. Sanvitto, "Vortex and half-vortex dynamics in a nonlinear spinor quantum fluid," Sci. Adv. **1**, e1500807 (2015).
26. F. Cardano, E. Karimi, L. Marrucci, C. De Lisio, and E. Santamato, "Violation of Leggett-type inequalities in the spin-orbit degrees of freedom of a single photon," Phys. Rev. A **88**, 032101 (2013).
27. A. Valles, V. D'Ambrosio, M. Hendrych, M. Micuda, L. Marrucci, F. Sciarrino, and J. Torres, "Generation of tunable entanglement and violation of a bell-like inequality between different degrees of freedom of a single photon," Phys. Rev. A **90**, 052326 (2014).
28. E. Nagali, L. Sansoni, F. Sciarrino, F. De Martini, L. Marrucci, B. Piccirillo, E. Karimi, and E. Santamato, "Optimal quantum cloning of orbital angular momentum photon qubits through Hong-Ou-Mandel coalescence," Nat. Photonics **3**, 720–723 (2009).
29. D. Bouwmeester, J. Pan, K. Mattle, M. Eibl, H. Weinfurter, and A. Zeilinger, "Experimental quantum teleportation," Nature **390**, 575–579 (1997).
30. D. Boschi, S. Branca, F. De Martini, L. Hardy, and S. Popescu, "Experimental realization of teleporting an unknown pure quantum state via dual classical and Einstein-Podolsky-Rosen channels," Phys. Rev. Lett. **80**, 1121–1125 (1998).
31. C. Hong, Z. Ou, and L. Mandel, "Measurement of subpicosecond time intervals between two photons by interference," Phys. Rev. Lett. **59**, 2044–2046 (1987).
32. V. D'Ambrosio, E. Nagali, S. Walborn, L. Aolita, S. Slussarenko, L. Marrucci, and F. Sciarrino, "Complete experimental toolbox for alignment-free quantum communication," Nat. Commun. **3**, 961–968 (2012).
33. G. Vallone, V. D'Ambrosio, A. Sponselli, S. Slussarenko, L. Marrucci, F. Sciarrino, and P. Villoresi, "Free-space quantum key distribution by rotation-invariant twisted photons," Phys. Rev. Lett. **113**, 060503 (2014).
34. A. Sit, F. Bouchard, R. Fickler, J. Gagnon-Bischoff, H. Larocque, K. Heshami, D. Elser, C. Peuntinger, K. Günthner, B. Heim, C. Marquardt, G. Leuchs, R. W. Boyd, and E. Karimi, "High-dimensional intracity quantum cryptography with structured photons," Optica **4**, 1006 (2017).
35. I. Nape, E. Otte, A. Vallés, C. Rosales-Guzmán, F. Cardano, C. Denz, and A. Forbes, "Self-healing high-dimensional quantum key distribution using hybrid spin-orbit Bessel states," Opt. Express **26**, 26946–26960 (2018).
36. B. Ndagano, B. Perez-Garcia, F. S. Roux, M. McLaren, C. Rosales-Guzman, Y. Zhang, O. Mouane, R. I. Hernandez-Aranda, T. Konrad,

and A. Forbes, "Characterizing quantum channels with non-separable states of classical light," Nat. Phys. **13**, 397–402 (2017).

37. V. D'Ambrosio, N. Spagnolo, L. Del Re, S. Slussarenko, Y. Li, L. Kwek, L. Marrucci, S. Walborn, L. Aolita, and F. Sciarrino, "Photonic polarization gears for ultra-sensitive angular measurements," Nat. Commun. **4**, 2432 (2013).

38. P. Zhang, B.-H. Liu, R.-F. Liu, H.-R. Li, F.-L. Li, and G.-C. Guo, "Implementation of one-dimensional quantum walks on spin-orbital angular momentum space of photons," Phys. Rev. A **81**, 052322 (2010).

39. F. Cardano, F. Massa, H. Qassim, E. Karimi, S. Slussarenko, D. Paparo, C. de Lisio, F. Sciarrino, E. Santamato, R. W. Boyd, and L. Marrucci, "Quantum walks and wavepacket dynamics on a lattice with twisted photons," Sci. Adv. **1**, e1500087 (2015).

40. H. B. Perets, Y. Lahini, F. Pozzi, M. Sorel, R. Morandotti, and Y. Silberberg, "Realization of quantum walks with negligible decoherence in waveguide lattices," Phys. Rev. Lett. **100**, 170506 (2008).

41. A. Peruzzo, M. Lobino, J. C. F. Matthews, N. Matsuda, A. Politi, K. Poulios, X.-Q. Zhou, Y. Lahini, N. Ismail, K. Worhoff, Y. Bromberg, Y. Silberberg, M. G. Thompson, and J. L. OBrien, "Quantum walks of correlated photons," Science **329**, 1500–1503 (2010).

42. L. Sansoni, F. Sciarrino, G. Vallone, P. Mataloni, A. Crespi, R. Ramponi, and R. Osellame, "Two-particle bosonic-fermionic quantum walk via integrated photonics," Phys. Rev. Lett. **108**, 010502 (2012).

43. A. Schreiber, A. Gabris, P. P. Rohde, K. Laiho, M. Stefanak, V. Potocek, C. Hamilton, I. Jex, and C. Silberhorn, "A 2D quantum walk simulation of two-particle dynamics," Science **336**, 55–58 (2012).

44. H. Defienne, M. Barbieri, I. A. Walmsley, B. J. Smith, and S. Gigan, "Two-photon quantum walk in a multimode fiber," Sci. Adv. **2**, e1501054 (2016).

45. X. Qi and S. Zhang, "Topological insulators and superconductors," Rev. Mod. Phys. **83**, 1057–1110 (2011).

46. T. Kitagawa, M. Broome, A. Fedrizzi, M. Rudner, I. Berg, E. Kassal, A. Aspuru-Guzik, E. Demler, and A. White, "Observation of topologically protected bound states in photonic quantum walks," Nat. Commun. **3**, 882 (2012).

47. F. Cardano and L. Marrucci, "Spin-orbit photonics," Nat. Photonics **9**, 776–778 (2015).

48. T. Kitagawa, M. S. Rudner, E. Berg, and E. Demler, "Exploring topological phases with quantum walks," Phys. Rev. A **82**, 033429 (2010).

49. F. Cardano, M. Maffei, F. Massa, B. Piccirillo, C. De Lisio, G. De Filippis, V. Cataudella, E. Santamato, and L. Marrucci, "Statistical moments of quantum-walk dynamics reveal topological quantum transitions," Nat. Commun. **7**, 11439 (2016).

50. F. Cardano, A. D'Errico, A. Dauphin, M. Maffei, B. Piccirillo, C. De Lisio, G. De Filippis, V. Cataudella, E. Santamato, L. Marrucci, M. Lewenstein, and P. Massignan, "Detection of Zak phases and topological invariants in a chiral quantum walk of twisted photons," Nat. Commun. **8**, 15516 (2017).

51. A. D'Errico, F. Cardano, M. Maffei, A. Dauphin, R. Barboza, C. Esposito, B. Piccirillo, M. Lewenstein, P. Massignan, and L. Marrucci, "Two-dimensional topological quantum walks in the momentum space of structured light," arXiv:1811.04001 (2018).

52. F. Cardano, E. Karimi, S. Slussarenko, L. Marrucci, C. De Lisio, and E. Santamato, "Polarization pattern of vector vortex beams generated by q-plates with different topological charges," Appl. Opt. **51**, C1–C6 (2012).

53. F. Cardano, E. Karimi, L. Marrucci, C. De Lisio, and E. Santamato, "Generation and dynamics of optical beams with polarization singularities," Opt. Express **21**, 8815–8820 (2013).

54. A. D'Errico, R. D'Amelio, B. Piccirillo, F. Cardano, and L. Marrucci, "Measuring the complex orbital angular momentum spectrum and spatial mode decomposition of structured light beams," Optica **4**, 1350–1357 (2017).

55. K. Toyoda, F. Takahashi, S. Takizawa, Y. Tokizane, K. Miyamoto, R. Morita, and T. Omatsu, "Transfer of light helicity to nanostructures," Phys. Rev. Lett. **110**, 143603 (2013).

56. L. Wong and F. Kartner, "Direct acceleration of an electron in infinite vacuum by a pulsed radially-polarized laser beam," Opt. Express **18**, 25035–25051 (2010).

57. D. Grier, "A revolution in optical manipulation," Nature **424**, 810–816 (2003).

58. R. Chen, K. Agarwal, C. Sheppard, and X. Chen, "Imaging using cylindrical vector beams in a high numerical-aperture microscopy system," Opt. Lett. **38**, 3111–3114 (2013).

59. R. Dorn, S. Quabis, and G. Leuchs, "Sharper focus for a radially polarized light beam," Phys. Rev. Lett. **91**, 233901 (2003).

60. W. Kimura, G. Kim, R. Romea, L. Steinhauer, I. Pogorelsky, K. Kusche, R. Fernow, X. Wang, and Y. Liu, "Laser acceleration of relativistic electrons using the inverse Cherenkov effect," Phys. Rev. Lett. **74**, 546–549 (1995).

61. B. Roxworthy and K. Toussaint, Jr., "Optical trapping with π-phase cylindrical vector beams," New J. Phys. **12**, 073012 (2010).

62. H. Wang, L. Shi, B. Lukyanchuk, C. Sheppard, and C. Chong, "Creation of a needle of longitudinally polarized light in vacuum using binary optics," Nat. Photonics **2**, 501–505 (2008).

63. A. Nesterov and V. Niziev, "Laser beams with axially symmetric polarization," J. Phys. D **33**, 1817–1822 (2000).

64. A. Abouraddy and K. Toussaint, Jr., "Three-dimensional polarization control in microscopy," Phys. Rev. Lett. **96**, 153901 (2006).

65. E. Karimi, F. Cardano, M. Maffei, C. De Lisio, L. Marrucci, R. Boyd, and E. Santamato, "Hardy's paradox tested in the spin-orbit Hilbert space of single photons," Phys. Rev. A **89**, 032122 (2014).

66. V. D'Ambrosio, E. Herbauts, I. Amselem, E. Nagali, M. Bourennane, F. Sciarrino, and A. Cabello, "Experimental implementation of a Kochen-Specker set of quantum tests," Phys. Rev. X **3**, 011012 (2013).

67. E. Karimi, G. Zito, B. Piccirillo, L. Marrucci, and E. Santamato, "Hypergeometric-Gaussian modes," Opt. Lett. **32**, 3053–3055 (2007).

68. D. Naidoo, F. Roux, A. Dudley, I. Litvin, B. Piccirillo, L. Marrucci, and A. Forbes, "Controlled generation of higher-order Poincaré sphere beams from a laser," Nat. Photonics **10**, 327–332 (2016).

69. M. Padgett, F. F. M. Miatto, M. Lavery, A. Zeilinger, and R. Boyd, "Divergence of an orbital-angular-momentum-carrying beam upon propagation," New J. Phys. **17**, 023011 (2015).

70. W. Cheng, J. Haus, and Q. Zhan, "Propagation of vector vortex beams through a turbulent atmosphere," Opt. Express **17**, 17829–17836 (2009).

71. P. Shumyatsky, G. Milione, and R. Alfano, "Optical memory effect from polarized Laguerre-Gaussian light beam in light-scattering turbid media," Opt. Commun. **321**, 116–123 (2014).

72. Y. Ren, G. Xie, H. Huang, N. Ahmed, Y. Yan, L. Li, C. Bao, M. Lavery, M. Tur, M. Neifeld, R. Boyd, J. Shapiro, and A. Willner, "Adaptive-optics-based simultaneous pre-and post-turbulence compensation of multiple orbital-angular-momentum beams in a bidirectional free-space optical link," Optica **1**, 376–382 (2014).

73. G. Milione, D. Nolan, and R. Alfano, "Determining principal modes in a multimode optical fiber using the mode dependent signal delay method," J. Opt. Soc. Am. B **32**, 143–149 (2015).

74. R. Black and L. Gagnon, *Optical Waveguide Modes: Polarization, Coupling and Symmetry* (McGraw-Hill, 2009).

75. V. Parigi, V. D'Ambrosio, C. Arnold, L. Marrucci, F. Sciarrino, and J. Laurat, "Storage and retrieval of vector beams of light in a multiple-degree-of-freedom quantum memory," Nat. Commun. **6**, 7706 (2015).

76. M. Krenn, R. Fickler, M. Fink, J. Handsteiner, M. Malik, T. Scheidl, R. Ursin, and A. Zeilinger, "Communication with spatially modulated light through turbulent air across vienna," New J. Phys. **16**, 113028 (2014).

77. O. Farias, V. D'Ambrosio, C. Taballione, F. Bisesto, S. Slussarenko, L. Aolita, L. Marrucci, S. Walborn, and F. Sciarrino, "Resilience of hybrid optical angular momentum qubits to turbulence," Sci. Rep. **5**, 8424 (2015).

78. P. Aspect, A. Grangier, and G. Roger, "Experimental tests of realistic local theories via Bell's theorem," Phys. Rev. Lett. **47**, 460–463 (1981).

79. V. D'Ambrosio, G. Carvacho, F. Graffitti, C. Vitelli, B. Piccirillo, L. Marrucci, and F. Sciarrino, "Entangled vector vortex beams," Phys. Rev. A **94**, 030304 (2016).

80. V. D'Ambrosio, F. Baccari, S. Slussarenko, L. Marrucci, and F. Sciarrino, "Arbitrary, direct and deterministic manipulation of vector beams via electrically-tuned q-plates," Sci. Rep. **5**, 7840 (2015).

81. Y. Yu, M. Nakano, and T. Ikeda, "Photomechanics: directed bending of a polymer film by light," Nature **425**, 145 (2003).

82. D. Kim, S. Tripathy, L. Li, and J. Kumar, "Laser-induced holographic surface relief gratings on nonlinear optical polymer films," Appl. Phys. Lett. **66**, 1166–1168 (1995).

83. A. Ambrosio, L. Marrucci, F. Borbone, A. Roviello, and P. Maddalena, "Light-induced spiral mass transport in azo-polymer films under vortex-beam illumination," Nat. Commun. **3**, 989 (2012).

84. A. Ambrosio, P. Maddalena, and L. Marrucci, "Molecular model for light-driven spiral mass transport in azopolymer films," Phys. Rev. Lett. **110**, 146102 (2013).

85. D. Chrisey and G. E. Hubler, *Pulsed Laser Deposition of Thin Films* (Wiley, 1994).

86. B. Neuenschwander, B. Jaeggi, M. Schmid, and G. Hennig, "Surface structuring with ultra-short laser pulses: basics, limitations and needs for high throughput," Phys. Procedia **56**, 1047–1058 (2014).

87. S. Musazzi and U. E. Perini, *Laser-Induced Breakdown Spectroscopy*, Series in Optical Sciences (Springer, 2014).

88. K. Anoop, R. Fittipaldi, A. Rubano, X. Wang, D. Paparo, A. Vecchione, L. Marrucci, R. Bruzzese, and S. Amoruso, "Direct femtosecond laser ablation of copper with an optical vortex beam," J. Appl. Phys. **116**, 113102 (2014).

89. K. Anoop, A. Rubano, R. Fittipaldi, X. Wang, D. Paparo, A. Vecchione, L. Marrucci, R. Bruzzese, and S. Amoruso, "Femtosecond laser surface structuring of silicon using optical vortex beams generated by a q-plate," Appl. Phys. Lett. **104**, 241604 (2014).

90. J. Nivas, S. He, A. Rubano, A. Vecchione, D. Paparo, L. Marrucci, R. Bruzzese, and S. Amoruso, "Direct femtosecond laser surface structuring with optical vortex beams generated by a q-plate," Sci. Rep. **5**, 17929 (2015).

91. J. Nivas, H. Shutong, K. Anoop, A. Rubano, R. Fittipaldi, A. Vecchione, D. Paparo, L. Marrucci, R. Bruzzese, and S. Amoruso, "Laser ablation of silicon induced by a femtosecond optical vortex beam," Opt. Lett. **40**, 4611–4614 (2015).

92. J. Nivas, F. Cardano, Z. Song, A. Rubano, R. Fittipaldi, A. Vecchione, D. Paparo, L. Marrucci, R. Bruzzese, and S. Amoruso, "Surface structuring with polarization-singular femtosecond laser beams generated by a q-plate," Sci. Rep. **7**, 42142 (2017).

93. J. Nivas, S. He, Z. Song, A. Rubano, A. Vecchione, D. Paparo, L. Marrucci, R. Bruzzese, and S. Amoruso, "Femtosecond laser surface structuring of silicon with Gaussian and optical vortex beams," Appl. Surf. Sci. **418**, 565–571 (2017).

94. J. Nivas, E. Allahyari, F. Cardano, A. Rubano, R. Fittipaldi, A. Vecchione, D. Paparo, L. Marrucci, R. Bruzzese, and S. Amoruso, "Surface structures with unconventional patterns and shapes generated by femtosecond structured light fields," Sci. Rep. **8**, 13613 (2018).

95. E. Allahyari, J. Nivas, F. Cardano, R. Bruzzese, R. Fittipaldi, L. Marrucci, D. Paparo, A. Rubano, A. Vecchione, and S. Amoruso, "Simple method for the characterization of intense Laguerre-Gauss vector vortex beams," Appl. Phys. Lett. **112**, 211103 (2018).

96. J. Bonse, S. Baudach, J. Krüger, W. Kautek, and M. Lenzner, "Femtosecond laser ablation of silicon-modification thresholds and morphology," Appl. Phys. Lett. **74**, 19–25 (2002).

97. K. Lou, S.-X. Qian, X.-L. Wang, Y. Li, B. Gu, C. Tu, and H.-T. Wang, "Two-dimensional microstructures induced by femtosecond vector light fields on silicon," Opt. Express **20**, 120–127 (2012).

98. M. Lax, W. Louisell, and W. McKnight, "From Maxwell to paraxial wave optic," Phys. Rev. A **11**, 1365–1370 (1975).

99. M. Scully, "A simple laser linac," Appl. Phys. B **51**, 238–241 (1990).

100. T. Bauer, S. Orlov, U. Peschel, P. Banzer, and G. Leuchs, "Nanointerferometric amplitude and phase reconstruction of tightly focused vector beams," Nat. Photonics **8**, 23–27 (2014).

101. B. Piccirillo, S. Slussarenko, L. Marrucci, and E. Santamato, "Directly measuring mean and variance of infinite-spectrum observables such as the photon orbital angular momentum," Nat. Commun. **6**, 8606 (2015).

102. B. Cvarch, B. Khajavi, J. Jones, B. Piccirillo, L. Marrucci, and E. Galvez, "Monstar polarization singularities with elliptically-symmetric q-plates," Opt. Express **25**, 14935–14943 (2017).

103. G. Ruane, G. Swartzlander, S. Slussarenko, L. Marrucci, and M. Dennis, "Nodal areas in coherent beams," Optica **2**, 147–150 (2015).

104. G. Foo, D. Palacios, and G. Swartzlander, "Optical vortex coronagraph," Opt. Lett. **30**, 3308–3310 (2005).

105. A. Aleksanyan and E. Brasselet, "Vortex coronagraphy from self-engineered liquid crystal spin-orbit masks," Opt. Lett. **41**, 5234–5237 (2016).

106. B. Piccirillo, M. Picardi, L. Marrucci, and E. Santamato, "Flat polarization-controlled cylindrical lens based on the Pancharatnam-Berry geometric phase," Eur. J. Phys. **38**, 034007 (2017).

107. S. Slussarenko, A. Alberucci, C. P. Jisha, B. Piccirillo, E. Santamato, G. Assanto, and L. Marrucci, "Guiding light via geometric phases," Nat. Photonics **10**, 571–575 (2016).

108. H. Rubinsztein-Dunlop, A. Forbes, M. Berry, M. Dennis, D. Andrews, M. Mansuripur, C. Denz, C. Alpmann, P. Banzer, T. Bauer, E. Karimi, L. Marrucci, M. Padgett, M. Ritsch-Marte, N. Litchinitser, N. Bigelow, C. Rosales-Guzmán, A. Belmonte, J. Torres, T. Neely, M. Baker, R. Gordon, A. Stilgoe, J. Romero, A. White, R. Fickler, A. Willner, G. Xie, B. McMorran, and A. Weiner, "Roadmap on structured light," J. Opt. **19**, 13001 (2017).

109. M. Rafayelyan and E. Brasselet, "Laguerre-Gaussian modal q-plates," Opt. Lett. **42**, 1966–1969 (2017).

110. E. Brasselet, "Tunable high-resolution macroscopic self-engineered geometric phase optical elements," Phys. Rev. Lett. **121**, 033901 (2018).

111. Y. Chen, J. Gao, Z.-Q. Jiao, K. Sun, W.-G. Shen, L.-F. Qiao, H. Tang, X.-F. Lin, and X.-M. Jin, "Mapping twisted light into and out of a photonic chip," Phys. Rev. Lett. **121**, 233602 (2018).

112. A. Alberucci, C. P. Jisha, L. Marrucci, and G. Assanto, "Electromagnetic confinement via spin-orbit interaction in anisotropic dielectrics," ACS Photon. **3**, 2249–2254 (2016).

113. C. P. Jisha, A. Alberucci, L. Marrucci, and G. Assanto, "Interplay between diffraction and the Pancharatnam-Berry phase in inhomogeneously twisted anisotropic media," Phys. Rev. A **95**, 023823 (2017).

114. A. Hernandez-Serrano, E. Castro-Camus, and D. Lopez-Mago, "Q-plate for the generation of terahertz cylindrical vector beams fabricated by 3D printing," J. Infrared Millim. Terahertz Waves **38**, 938–944 (2017).

115. A. Minasyan, C. Trovato, J. Degert, E. Freysz, E. Brasselet, and E. Abraham, "Geometric phase shaping of terahertz vortex beams," Opt. Lett. **42**, 41–44 (2017).

116. C. Loussert, K. Kushnir, and E. Brasselet, "Q-plates micro-arrays for parallel processing of the photon orbital angular momentum," Appl. Phys. Lett. **105**, 121108 (2014).

117. M. G. Nassiri and E. Brasselet, "Multispectral management of the photon orbital angular momentum," Phys. Rev. Lett. **121**, 213901 (2018).